Elastic Light Scattering from Silica and Silicon Microresonators

by

Ersin Hüseyinoğlu

A Thesis Submitted to the
Graduate School of Sciences and Engineering
in Partial Fulfillment of the Requirements for
the Degree of

Master of Science

in

Materials Science and Engineering

Koç University

August 2011

Koç University

Graduate School of Sciences and Engineering

This is to certify that I have examined this copy of a master's thesis by

Ersin Hüseyinoğlu

and have found that it is complete and satisfactory in all respects,
and that any and all revisions required by the final
examining committee have been made.

Committee Members:

_____

Ali Serpengüzel, Ph. D. (Advisor)

_____

Özgür Birer, Ph. D.

_____

Şükrü Ekin Kocabaş, Ph. D.

Date: _____

ABSTRACT

Optical microresonators are gaining an important role in a variety of applications such as sensing, novel light source, and optical communication applications. Lightwave circuits are already using these optical microresonators extensively.

Silicon being the main material for the current electronic integrated circuits can also be used for producing future photonic integrated circuits or photonic optoelectronic circuits. These photonic integrated circuits can easily upgrade their electronic counterparts, using the well developed CMOS process technology.

This work covers simulation and analysis of the elastic light scattering from various silica silicon microresonators such as microslabs, microcylinders, microspheres, and microspheroids. Absorption, extinction, and scattering efficiencies as well as elastic scattering intensities are calculated and analyzed for silica and silicon microresonators. The resulting morphology dependent resonances, which are apparent in the elastic scattering spectra, can have novel applications in silicon photonics.

ÖZET

Optik mikroçınlaçlar, algılama, ışık kaynağı ve optik iletişim gibi uygulamalar için gittikçe daha fazla önem kazanmaktadır. Optik devreler, şu anda optik mikroçınlaçları kullanmaktadır.

Günümüzde kullanılan elektronik tümleşik devrelerin ana gereci olan silisyum, gelecekte de fotonik tümleşik ve fotonik optoelektronik tümleşik devrelerin üretilmesinde kullanılabilir. Geliştirilmiş CMOS teknolojisini kullanarak üretilecek bu fotonik tümleşik devreler, elektronik tümleşik devrelerin yerini kolayca alabilirler.

Bu çalışma, mikroplaka, mikrosilindir, mikroküre ve mikroküremsi gibi çeşitli silika ve silisyum mikroçınlaçlardan esnek ışık saçılımı benzeşimlerini ve incelemelerini içermektedir. Silika ve silisyum mikroçınlaçlar için saçılım şiddetinin yanı sıra soğurma, sönüm ve saçılım verimleri de hesaplanmıştır.

Esnek saçılım izgelerinde görünen yapı tabanlı kipler, silisyum fotonik alanında yeni uygulamalar geliştirmek için kullanılabilir

ACKNOWLEDGEMENTS

First of all, I would like to thank my advisor, Prof. Ali Serpengüzel for his guidance, understanding and patience during my M.Sc. degree study in Koç University. I am grateful to him for giving me the chance of working in his group in the Koç University Microphotonics Research Laboratory.

I would like to thank Asst. Prof. Özgür Birer and Asst. Prof. Şükrü Ekin Kocabaş for their participation to my thesis committee and their valuable feedback.

I would like to thank Profs. Peter W. Barber and Steven C. Hill for providing the software, included in their book "Light scattering by particles: Computational Methods."

I would also like to indicate my deep gratitude to my friends and colleagues in Koç University; Emre Yüce, Mohammed Sharif Murib, Hasan Yılmaz, Hande Öztürk, Kurt David Webb, Ceren Yılmaz, Huzeyfe Yılmaz, Ulaş Sabahattin Gökay, Yasemin Yar, and Seyed Alireza Aleali, for their supportive friendship, and valuable scientific discussions.

I would like to acknowledge Türkiye Bilimsel ve Teknolojik Araştırma Kurumu (TÜBİTAK) grant No. EEEAG - 106E215 for partial support of our research in the Koç University Microphotonics Research Laboratory.

Finally, and most importantly, I want to express my gratitude to my parents, my sister, and my brother, for their endless love, care, advices and support throughout my life.

This thesis is dedicated to my parents, my sister; Serap, and my brother; Erdem.

TABLE OF CONTENTS

LIST OF FIGURES

NOMENCLATURE

n	Mode Number
l	Mode order
m	Azimuthal more number
λ	Wavelength of light in vacuum
N	Refractive index of the medium
N_1	Refractive index of the resonator
a	Radius of the microresonator
x	Size parameter
M	Relative refractive index
k	Propagation vector
Q_{ext}	Extinction efficiency
Q_{sca}	Scattering efficiency
Q_{abs}	Absorption efficiency
C_{geo}	Geometrical cross section
C_{ext}	Extinction cross section
C_{sca}	Scattering cross section
C_{abs}	Absorption cross section
θ	Polar angle from z-axis
c	Speed of light in vacuum
Δx	Mode spacing
$\Delta \upsilon$	Mode spacing in frequency domain
$\Delta \lambda$	Mode spacing in wavelength domain
δx	Mode splitting
ϕ	Azimuthal angle
$E_{\perp}$	Perpendicular electric field
$E_{//}$	Parallel electric field

"Dünyada her şey için, medeniyet için, hayat için, muvaffakiyet için en hakiki mürşit ilimdir, fendir. İlim ve fennin haricinde mürşit aramak, gaflettir, cehalettir, dalalettir."

Mustafa Kemal Atatürk
(22.09.1924, Samsun, Türkiye)

Chapter 1

INTRODUCTION

The optical modes or optical resonances are analogous to the acoustic whispering gallery modes, which were first proposed by Lord Rayleigh in 1912 [1], for optical frequency range. Optical resonators are physical structures that localize the incident light by total internal reflection, and therefore manifest morphology dependent resonances. Pioneering research on the subject had been performed by A. Ashkin *et al* [2-4], R.K. Chang *et al* [5], and S.C. Hill *et al* [6]. Moreover, several books were published that cover the elastic light scattering from particles, and morphology dependent resonances (MDR's) [7-13]. Microresonators' MDR's are being used widely in photonics [14, 15].

Being a basic building block for photonics, resonators attracted a lot of attention, and extensive research had been done on the subject [16-20]. Several geometries can be used as microresonators such as microslabs, microdisks, microrings, microtoroids, microspheres, and photonic crystal microcavities in order to localize light [16]. Recently, due to the need for better photonic devices for high speed communication, several applications have been developed regarding novel light sources [21-28], wavelength conversion [29], optical filters [30-38], switches [32, 39], modulators [40-42], sensors [43-51], optical frequency comb generation [52], and electrophoresis [53]. In addition to these applications, photonic integrated circuits can be achieved by implementation of some or all of these applications.

After the proposal of integrated optics by S.E. Miller [54], the photonic integrated circuits have been pursued [55-58], since the transmission and processing of light is an intriguing idea that bundles high speed communications along with high speed processing.

Silicon is a good candidate for photonic integrated circuits due to several reasons [59, 60]. Silicon is an abundant, well-understood, and a cheap material, that is suitable for mass production [59], which makes it a widely used material in

electronics. Silicon is also suitable for photonics [60] and therefore, can be an important material for photonic integrated circuits.

Due to this importance, elastic light scattering experiments were performed in silicon microspheres, and numerical simulations were performed to support the experimental results. The computer programs, which were used in the calculations, were provided with the book by P.W. Barber and S.C. Hill [11] by using FORTRAN programming language. The experimental data was collected with National Instruments LabVIEW® software.

Chapter 2 includes a brief introduction to optical resonators, and covers calculations of reflected and transmitted light intensities from both silicon and silica microslab resonators.

Silica and silicon cylindrical microresonators are investigated in chapter 3. Scattering, absorption and extinction efficiencies are calculated, as well as the scattering intensities for forward, elastic and backward scattering.

In chapter 4, the elastic light scattering from the spherical microresonator geometries are investigated for silica and silicon materials. In addition to the calculations the experimental elastic light scattering results from a silicon spherical resonator are presented.

Chapter 5 covers scattering efficiency calculations from silica, silicon nitride and silicon spheroid microresonators. In addition to scattering efficiency calculations, mode separation with the deformation of spherical geometry is investigated.

Chapter 6 concludes the work, and suggests future work that can be done to complete, or extend the understanding for elastic light scattering from silicon microresonators.

Chapter 2

SLAB MICRORESONATORS

Optical resonators confine light by morphology dependent resonances. Resonances occur, if the constructive interference condition is met:

$$\text{Optical Path Length} = n\lambda \qquad (2.1),$$

where n is the mode number and λ the wavelength of light in vacuum. These resonances are referred to as morphology dependent resonances, since they depend on the morphology of the resonator [10].

Elastic light scattering from particles, which have a smaller sizes than the wavelength of light, is called Rayleigh scattering. L.V. Lorenz [61] and G. Mie [62] independently solved the scattering problem for relatively bigger particles with sizes bigger then or comparable to the wavelength of light [63]. The Lorenz-Mie solution for plane waves is called Lorenz-Mie theory, and the solution for arbitrarily shaped beam excitation is referred as the generalized Lorenz-Mie theory.

The first studied geometry for resonator is a slab. The silica and silicon wafers and thin films can be modeled as microslab resonators.

2.1. Slab Resonator

Slab resonator is a special case of the Fabry-Perot resonator [64]. When a plane wave is incident on the slab resonator, a portion of the incident light is reflected back due to the Fresnel reflection, and rest of the light enters into the resonator. Within the resonator medium, the light travels back and forth, and if the resonance conditions are met, constructively interfered waves are transmitted through the resonator.

The simulated slab resonator is given in figure 2.1. The simulations are done with the FORTRAN programs, which are provided with the book by P.W. Barber and

S.C. Hill [11]. For a resonator that is illustrated in figure 2.1, the resonance condition is:

$$4aN_1 = n\lambda \tag{2.2},$$

where N_1 is the refractive index of the resonator medium, n the mode number, and λ is the wavelength of light in vacuum.

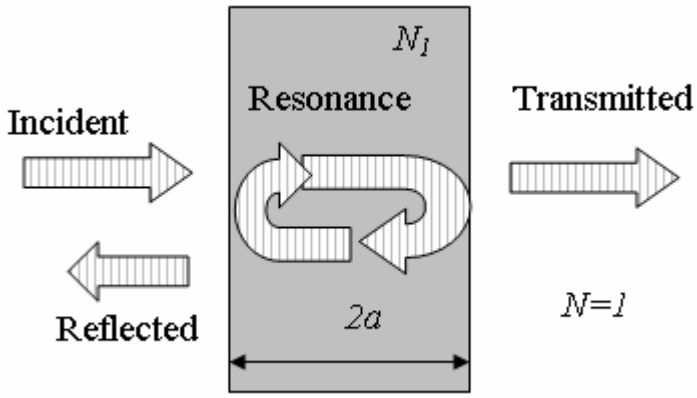

Figure 2.1: Slab Resonator Configuration.

A size dependent parameter can be defined for the resonator as the *size parameter*. The size parameter is the product of the propagation vector in the outside medium with the resonator's spatial parameter [11]:

$$x = ka \tag{2.3},$$

where, the propagation vector is:

$$k = \frac{2\pi N}{\lambda} \tag{2.4},$$

where, N is the refractive index of the external medium (environment) and λ the wavelength of light in the vacuum. Size parameter is a dimensionless parameter which, depends on the size, and the refractive index of the resonator, and also the wavelength of the incident light.

Also, the refractive index ratio should be defined for further use:

$$M \equiv \frac{N_1}{N} \qquad (2.5).$$

2.2. Silica Microslab

A silica slab model is used for calculating the spectra in figures 2.2, 2.3, 2.4, and 2.5. The thickness of the slab is chosen to be 2*a*. The transmitted light intensity through the slab and the reflected light intensity from the slab resonator are plotted in figure 2.2. The refractive index of the silica slab is chosen to be 1.50+*i*0.00. The incident light intensity is 1 (unity, or 100%).

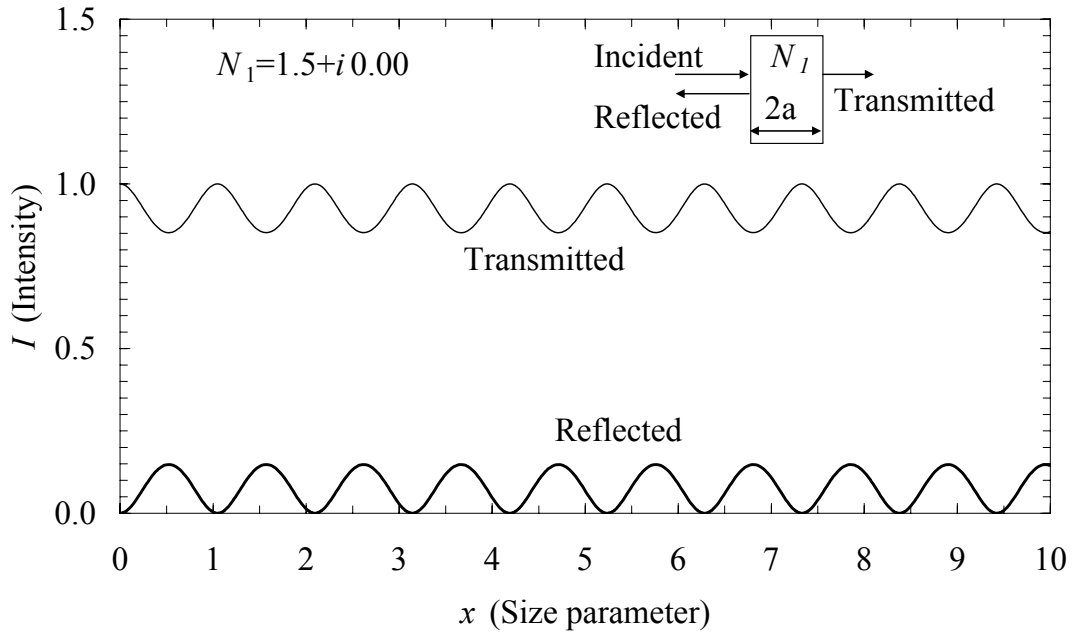

Figure 2.2: Transmitted and reflected intensities for a transparent silica slab.

The refractive index of the silica does not have any imaginary part, so there is no absorption, and the sum of the reflected and the transmitted light intensities equals to unity. The silica has a refractive index of 1.5, and due to the Fresnel reflections from the two surfaces, the reflectance from air-silica interfaces increases to 8% [63].

In figure 2.2, the average reflected light intensity is 8%. The resonant size parameters can be found by combining equations 2.2 and 2.3, which gives:

$$n = \left(\frac{2m}{\pi}\right)x \qquad (2.6).$$

For integer multiples of $\pi/2m$, there is a complete transmission of light through the resonator, therefore, the reflected light intensity decreases to zero. For silica with a refractive index of 1.5, the resonant size parameters are the integer multiplies of $\pi/3$.

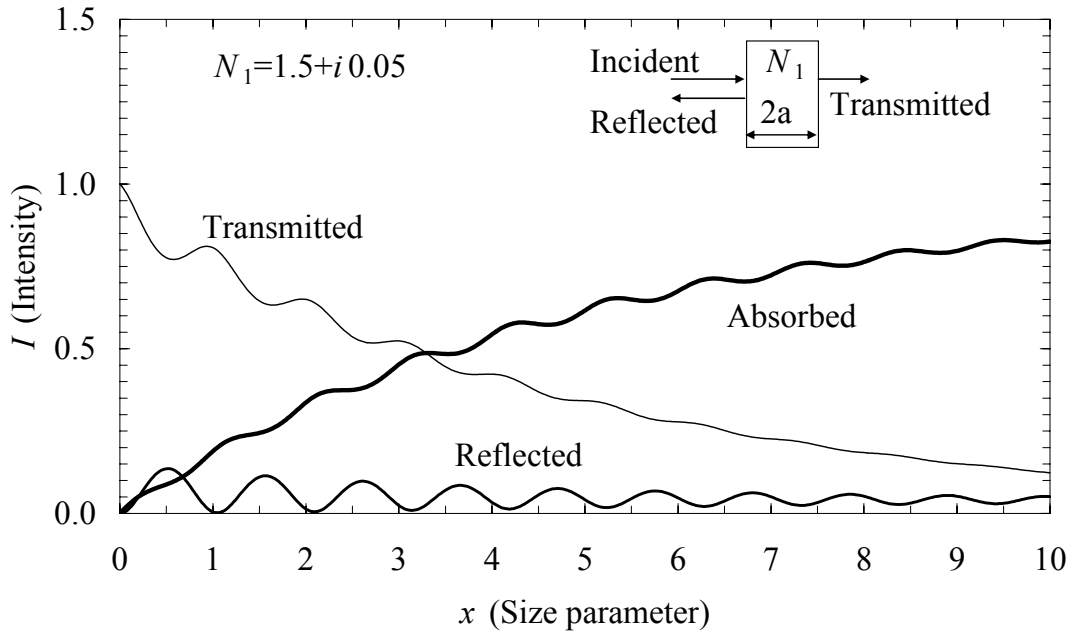

Figure 2.3: Transmitted, reflected, absorbed intensities for an absorbing silica slab.

In figure 2.3, the complex refractive index of the silica is taken as 1.5+i0.05, and the thickness of the slab is again 2a. As in the previous simulation, the incident light intensity is unity in this simulation. Although the sum of the transmitted and reflected light intensities do not equal to the incident light intensity, since there is absorption in silica, that is represented by the imaginary part of the refractive index.

As the trip length of light inside of the slab increases, the material absorbs more; therefore, both transmitted and reflected light intensities decrease as size parameter increases.

The relative internal intensities for a silica slab with a non-resonant size parameter of 11 are shown in figure 2.4 for both transparent and absorptive silica. Slab thickness is chosen to be 2*a*.

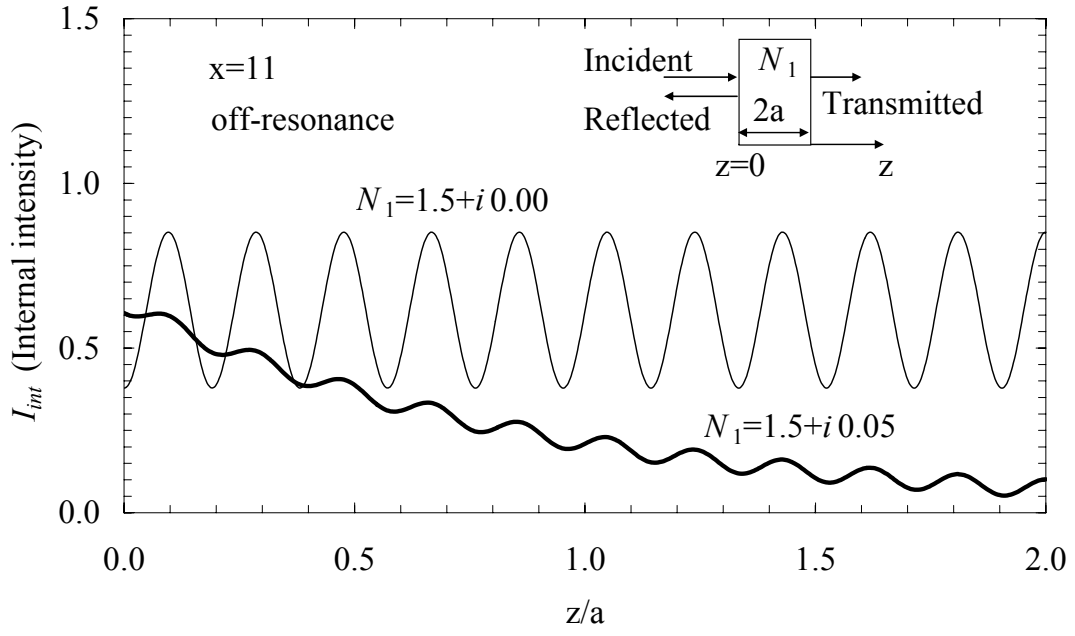

Figure 2.4: Relative internal intensities for silica slab for x=11.

As can be seen, there is no resonance, when the size parameter is 11, since the size parameter is not an integer multiple of $\pi/3$. Therefore, the internal light intensity is low. As expected, the internal intensity decreases with increasing slab thickness for the absorbing medium, which has a complex refractive index. However, the internal intensity is not decreasing in the transparent medium.

The relative internal intensities for a silica slab with a resonant size parameter of 4π are shown in figure 2.5 for both transparent and absorptive silica. Slab thickness is chosen to be 2*a*.

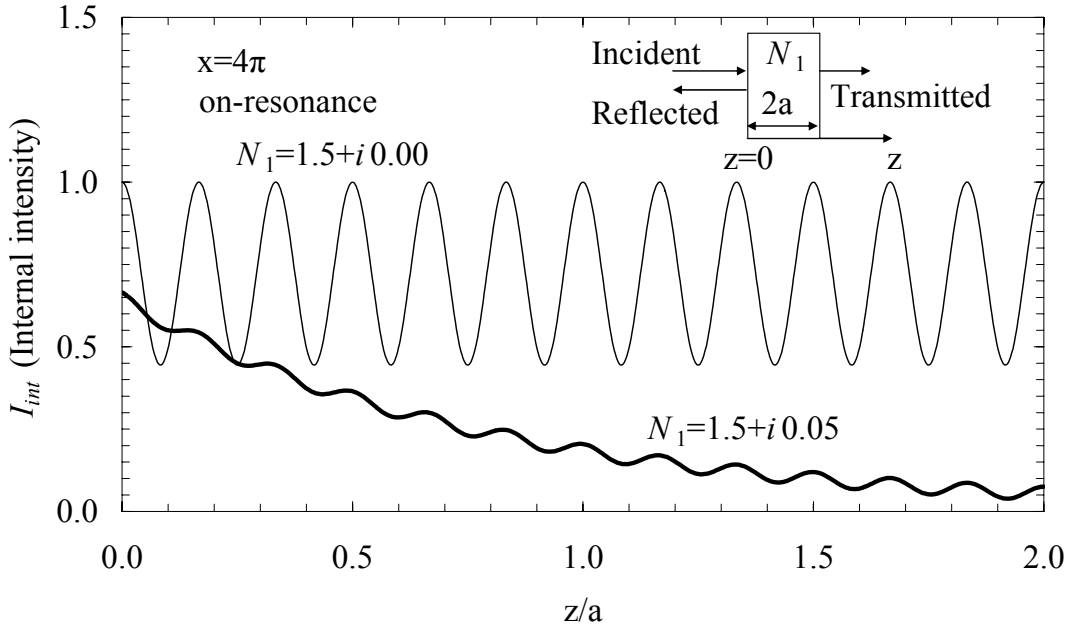

Figure 2.5: Relative internal intensities for silica slab for x=4π.

For a size parameter of 4π, which is an integer multiple of $\pi/3$, the fields are on resonance. Therefore the internal intensity for the slab with size parameter of 4π is higher than the internal intensity for the slab with a size parameter of 11. For transparent and absorbing media, the resonances can be seen, but in the absorbing medium, as expected, the light intensity tends to decrease as slab thickness increases, due to the absorption.

2.3. Silicon Microslab

Calculations are performed for a silicon slab with a thickness of 2*a*. The refractive index of 3.50+*i*0.00 is used for the calculations shown in figure 2.6.

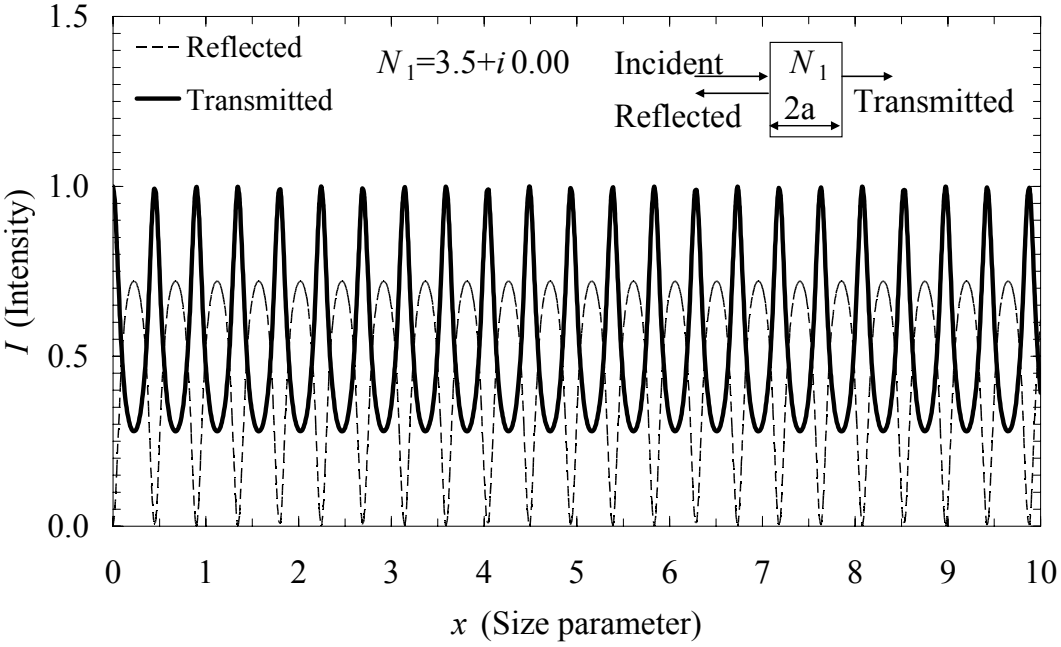

Figure 2.6: Transmitted and reflected intensities for a transparent silicon slab.

As the refractive index is increased to 3.5 from 1.5, the number of modes increased. The reflectance of air-silicon interface is around 31% [66]. Due to the multiple surface the reflectance increases to 47%, which is the value of average reflected light intensity in the figure 2.6. For the silicon slab, the intensity difference between the peaks and dips is relatively bigger than the silica with a refractive index of 1.5. Also, the sum of the reflected light intensity and transmitted light intensity is equal to the incident light intensity, which is unity (100%), since there is no absorption. The resonant size parameters should be integer multiples of $\pi/7$, for a silicon slab resonator. Therefore, increased number of modes is observed for the silicon resonator, as expected.

To simulate an absorption case, an imaginary part is added to the refractive index of 3.5 and the computation is performed for a refractive index of 3.5+*i*0.05 with the same configuration with the previous slab.

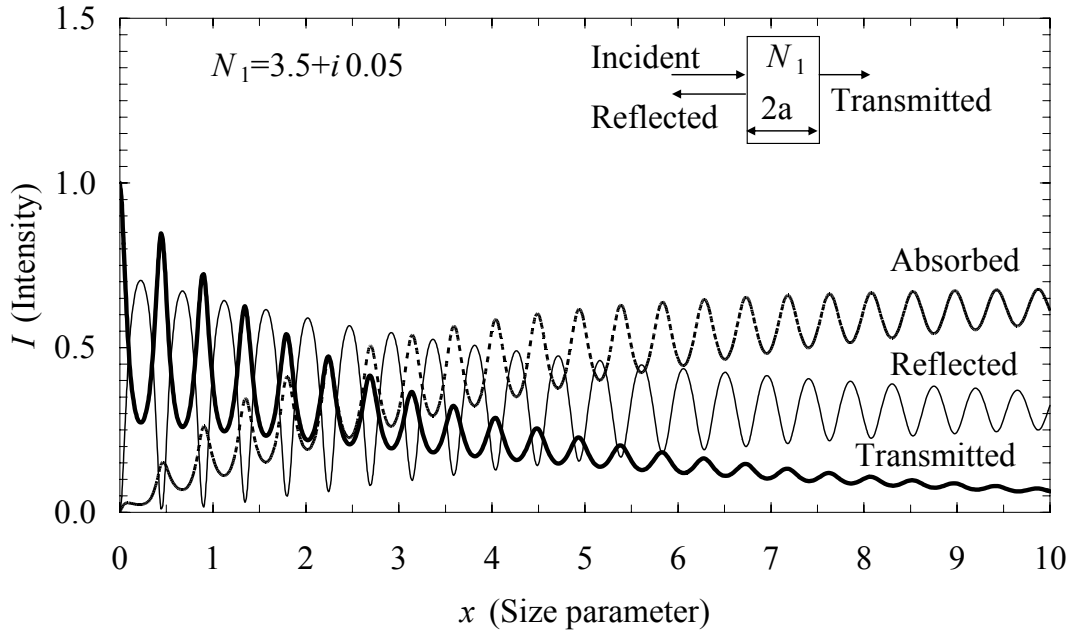

Figure 2.7: Transmitted, reflected, absorbed intensities for absorbing silicon slab.

The incident light intensity is unity. With the addition of imaginary part to the refractive index, the absorption is introduced, so the sum of the reflected and the transmitted light intensities is no longer equal to unity. Similar to the silica slab, the reflected and the transmitted light intensities decreases with increasing size parameter, although, the intensity difference between the peaks and dips are higher due to the higher reflectance of the silicon. The number of modes is the same as the transparent silicon slab.

The relative internal intensities are investigated for size parameters of 11 (non-resonant) and 4π (resonant). The silicon slab thickness is taken as 2*a*.

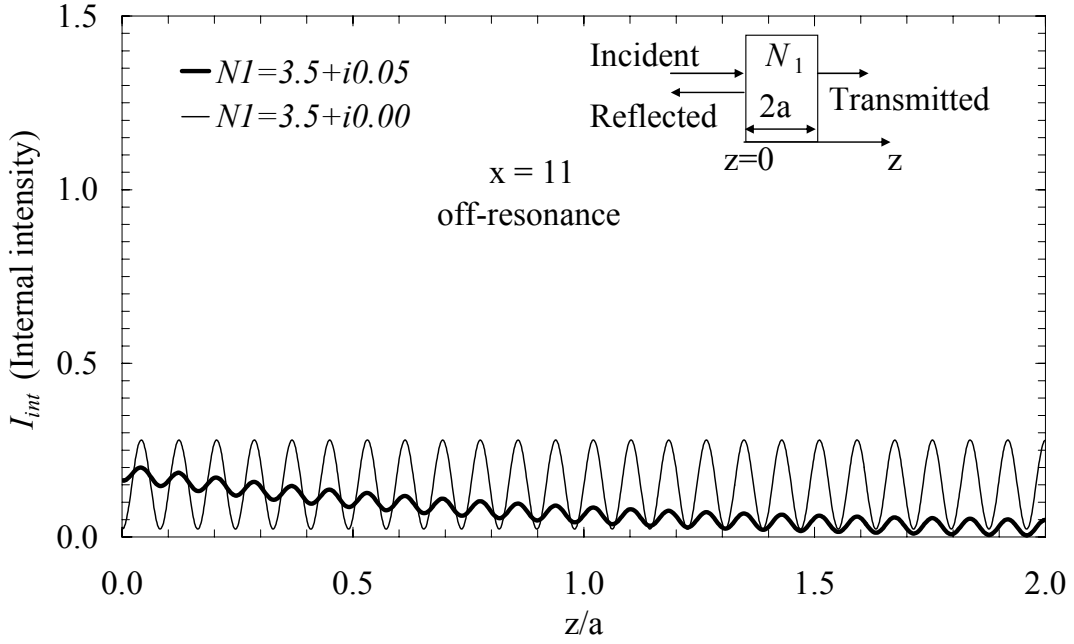

Figure 2.8: Relative internal intensities for silicon slab with x=11.

In figure 2.8, the size parameter of a silicon slab is 11, so the resonance condition is not satisfied. Therefore, the fields are not on resonance, so the internal light intensity is low. As expected, the average intensity is not changing with the increasing slab thickness for transparent silicon, while the average intensity decreases for increasing thickness of absorbing silicon.

In figure 2.9, the relative internal intensities are investigated for size parameter of 4π for a slab resonator with the same thickness of a $2a$. The resonant fields cause higher internal light intensity.

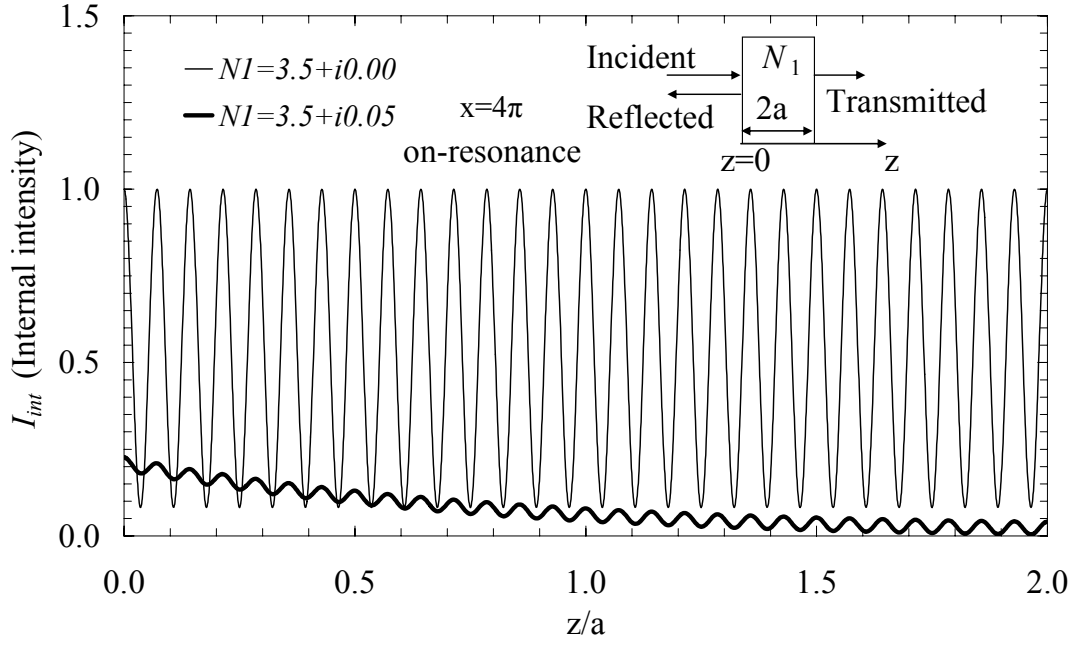

Figure 2.**9**: Relative internal intensities for silicon slab for x=4π.

So, as can be observed in both silica and silicon microslab resonators, the resonances can only be observed at certain size parameters. Therefore, it can be said that morphology dependent resonances for a specific resonator can be accessed for only certain wavelengths. The spectral density of resonances in silica slab is less than the spectral density of resonances in silicon due to the difference in refractive indices. As can be observed, the spectral density of resonances increases as refractive index increases. Another observation is the intensity difference between the off-resonance and on-resonance cases. Higher reflectance causes more reflection for off-resonance, but if the resonance condition is met, due to the zero reflection, the transmission intensity is maximized.

Chapter 3

CYLINDRICAL MICRORESONATORS

The next resonator geometry is the cylinder, which can be a model for optical fibers in the transverse direction. Optical fibers are extensively used in communication systems and going to be used in photonic integrated circuits for both inter- and intra-chip connections.

3. 1 Cylindrical Resonator

For two dimensional calculations an infinitely long cylinder is chosen. The circular cylinder is illuminated with an incident plane wave and several simulations are performed for different refractive indices and different size parameters. The following figure shows the configuration used for simulations.

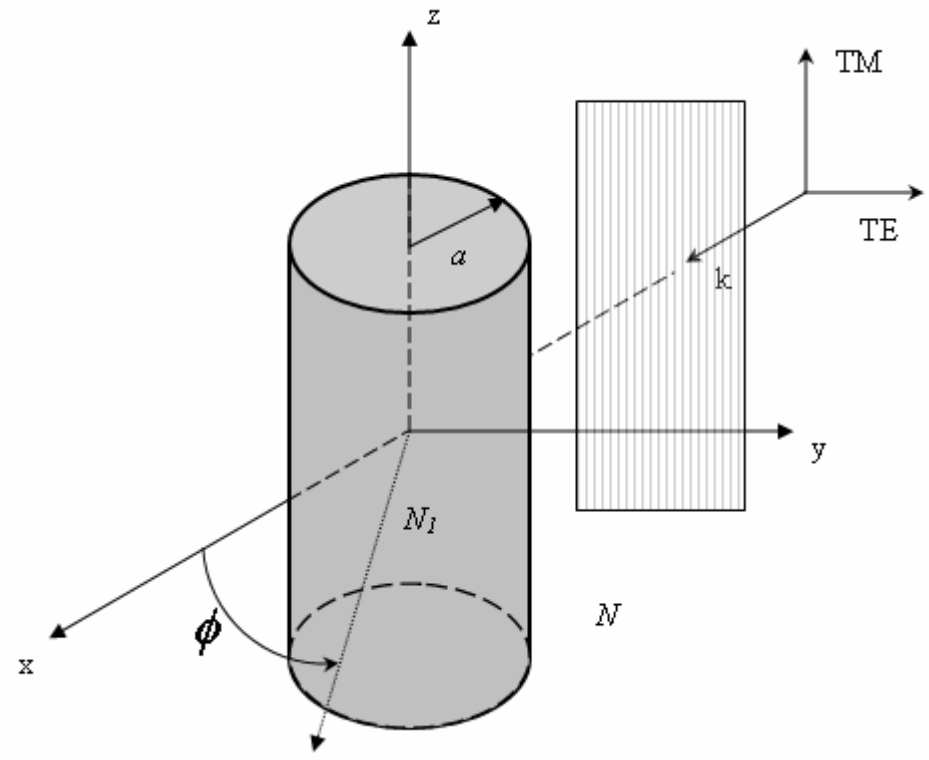

Figure 3.1: Cylindrical resonator configuration.

The resonance condition for cylindrical cylinder resonator can be defined as:

$$2\pi a N_1 = n\lambda \tag{3.1}.$$

By replacing size parameter into the equation 3.1, the following equation is gathered:

$$n = Mx \tag{3.2}.$$

Equation 3.2 means that, at every size parameter of x for integer multiples of $1/M$, there is a resonant mode. The term of scattering for cylindrical and spherical resonators are used instead of reflection and transmission. Both scattering and absorption removes energy from the incident wave, so scattering and absorption are the two components of extinction. Therefore, the sum of the scattering efficiency and absorption efficiency should give extinction efficiency [7]:

$$Q_{ext} = Q_{sca} + Q_{abs} \tag{3.3}.$$

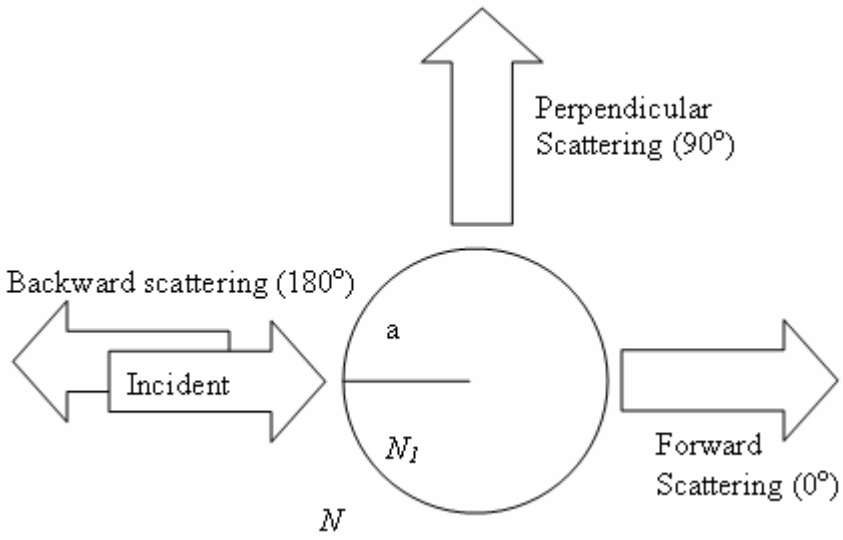

Figure 3.2: Scattering from a cylindrical resonator (top view).

Silica and silicon with respective refractive indices of 1.5 and 3.5 are studied for the cylindrical geometry. Efficiency factors are calculated, and simulations for scattering intensities at different angles are performed for both silica and silicon.

3.2 Silica Microcylinder

In the following simulation, silica with a refractive index of $1.5+i0.01$ is used in the cylindrical geometry. The radius of the silica cylinder is a. Scattering, absorption and extinction efficiencies are computed for an incident plane wave with TM polarization.

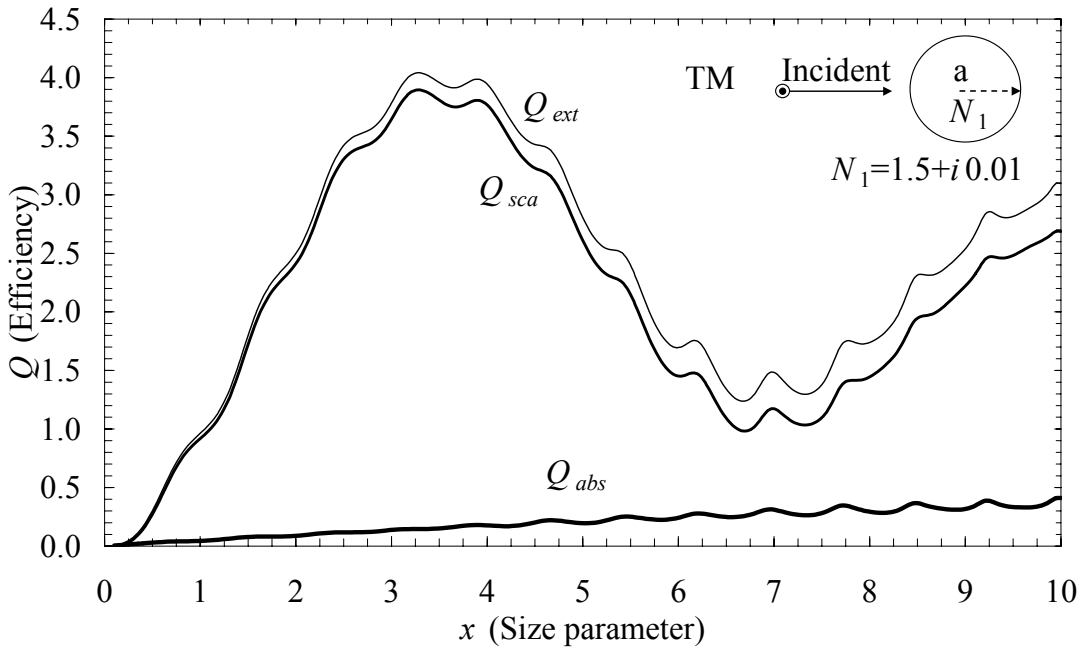

Figure 3.3: Extinction, scattering and absorption efficiencies for a silica cylinder.

In figure 3.3, extinction, scattering and absorption efficiencies (efficiency factors) are plotted. As can be observed initially, absorption efficiency is increasing with increasing size parameter, while the scattering efficiency is oscillating with the size parameter. As a sum of these two efficiencies, the extinction efficiency is also oscillating with the size parameter, since the scattering efficiency is the larger contributor to the extinction. In addition to this assessment, a peak for scattering and

extinction efficiencies are observed with a value of approximately of 4.0. The resonance peaks are identified on the oscillation structure.

In the next figure, scattering efficiencies for different polarizations of light is shown. The refractive index is chosen as 1.5+*i*0.00. The radius of the silica cylinder is *a*.

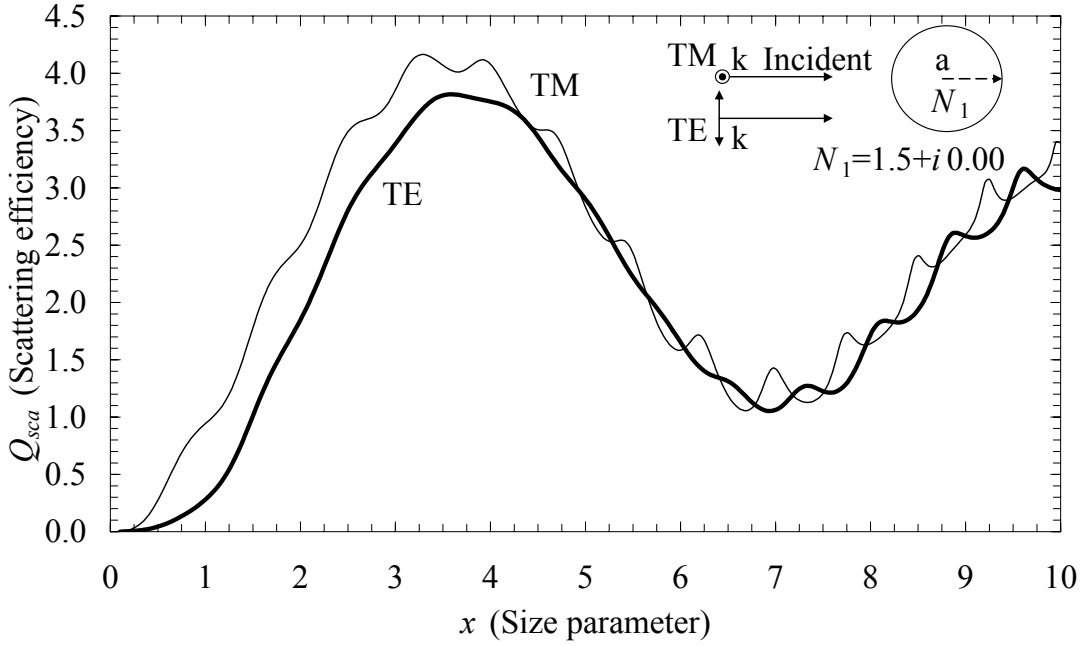

Figure 3.4: Scattering efficiencies for a silica cylinder.

In figure 3.4, the difference between the scattering efficiencies for TE and TM polarizations are shown. The oscillation behavior is similar for both polarizations, however scattering efficiency curve for TE polarization seems to follow scattering efficiency curve for TM polarization with a lag. This difference is caused by the refractive index experienced by the fields. As defined in figure 3.1, the TM and TE polarizations are experiencing different effective refractive indices. While TM polarization experiences more of the refractive index of the silica cylinder, TE polarization experiences less of the refractive index of silica, and more of the refractive index of environment (which is air in these calculations), thereby leading to weaker confinement, and a larger effective size parameter.

In figure 3.5, the scattering efficiency for TM polarization is investigated for size parameters between 15 and 20. The simulation is performed for a transparent silica cylinder with a refractive index of 1.5.

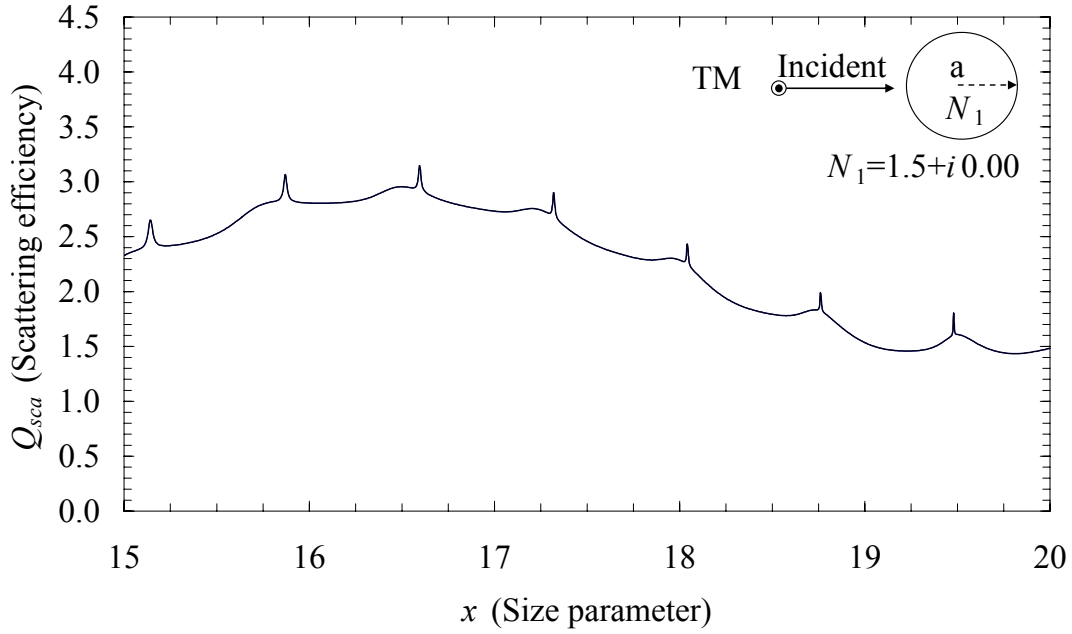

Figure 3.5: TM scattering efficiency for silica cylinder.

As can be observed in figure 3.5, distinguishable and narrower resonant peaks occur for higher size parameters. The oscillation behavior of the scattering efficiency, though it is damped noticeably, continues as size parameter increases. Moreover, the scattering efficiency seems to oscillate around the value of 2.0, which is still quite high for an efficiency which is normally expected to be 1.0.

The limiting value of 2.0 for extinction efficiency, which is referred as "*extinction paradox"* in some sources [7, 8, and 13] should be addressed. The extinction efficiency (Q_{ext}) is defined as the ratio of the extinction cross section (C_{ext}) to the geometrical cross sectional area (C_{geo}).

$$Q_{ext} = C_{ext} / C_{geo} \tag{3.4}.$$

Similarly, the scattering efficiency, and the absorption efficiency are the ratios of the scattering cross section and absorption cross sections to the geometrical cross sectional area. The extinction cross section is the energy removed from the original incident wave on the area of the resonator [7]. "*Cross sections"* are, generally, the functions of the state of polarization of the incident light, and the orientation of the resonator [7]. So, normalizing the extinction cross section with the geometrical cross section area gives the extinction efficiency. The normalization should give a limit of 1.0.

However, due to the diffraction pattern, additional energy is also removed from the incident wave, which gives diffraction with the same cross section of C_{geo}. Therefore, due to the Babinet's principle [7], the total extinction cross section is twice of the extinction cross section that is caused by both scattering and absorption. Thus, doubling the cross section, and using the same geometrical cross section area, leads to the limit value of 2.0 for the extinction efficiency. The oscillation behavior is caused by the interference of the incident (transmitted) wave and the scattered (diffracted) wave. Due to this interference, the oscillation occurs around the limiting value of 2.0, and it is called as interference structure [8].

The final property, that can be observed on the efficiency curve is the ripple structure. The peaks on the oscillation structure are called ripples, and they are the result of the resonant electromagnetic fields [13], and known as morphology dependent resonances (MDR's).

The scattering intensities for different polar angles are calculated and plotted. The incident beam has TM polarization, and the refractive index of the transparent silica cylinder is $1.5+i0.00$. The radius of the silica cylinder is chosen to be a. In figure 3.6, the forward scattering is shown, while the perpendicular scattering is plotted in figure 3.7. In figures 3.8, and 3.9, the backward scattering is simulated.

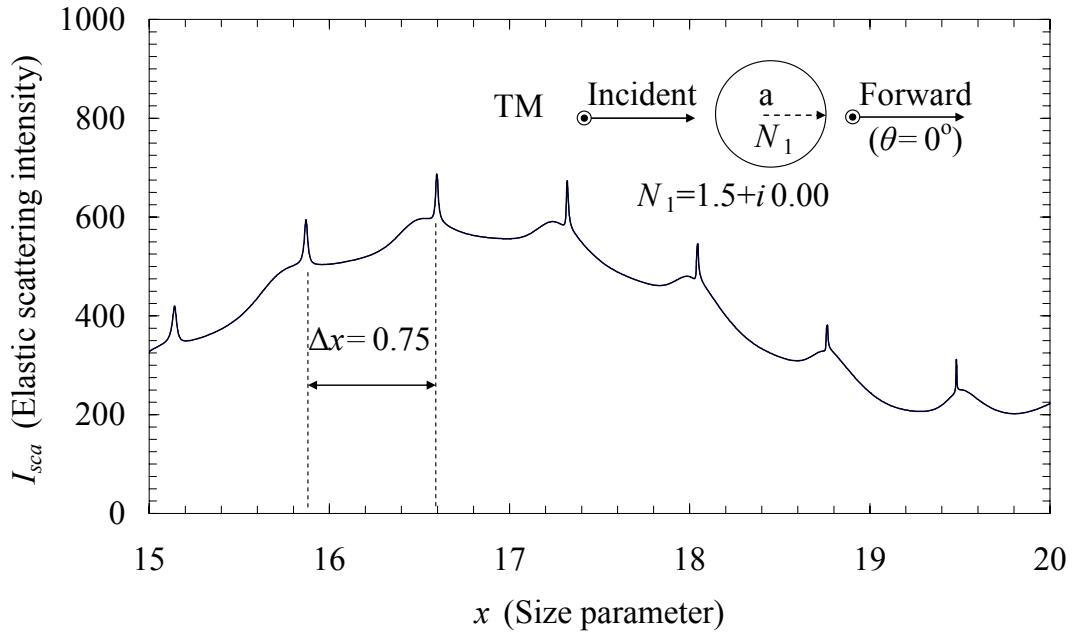

Figure 3.6: TM forward scattering intensity for silica cylinder.

In figure 3.6, the TM forward scattering intensity has a background due to the incident plane wave intensity. The MDR's have narrower peaks at higher size parameters. The mode spacing between the two consecutive modes with the same mode order can be calculated by simplifying the formula:

$$\frac{\Delta x}{x} = \frac{\Delta \upsilon}{\upsilon} \tag{3.5},$$

where, υ is the frequency of light in the vacuum, Δx the mode spacing, and $\Delta \upsilon$ the spacing between modes in frequency domain:

$$\Delta \upsilon = \frac{c}{2\pi a N_1} \tag{3.6}.$$

By simplifying the equation 3.5, by replacing the size parameter, and the mode spacing, equation 3.7 is gathered:

$$\Delta x = \frac{1}{M} \tag{3.7}.$$

The mode spacing is calculated as 0.75 for silica by using equation 3.7, and is in agreement with the simulation results.

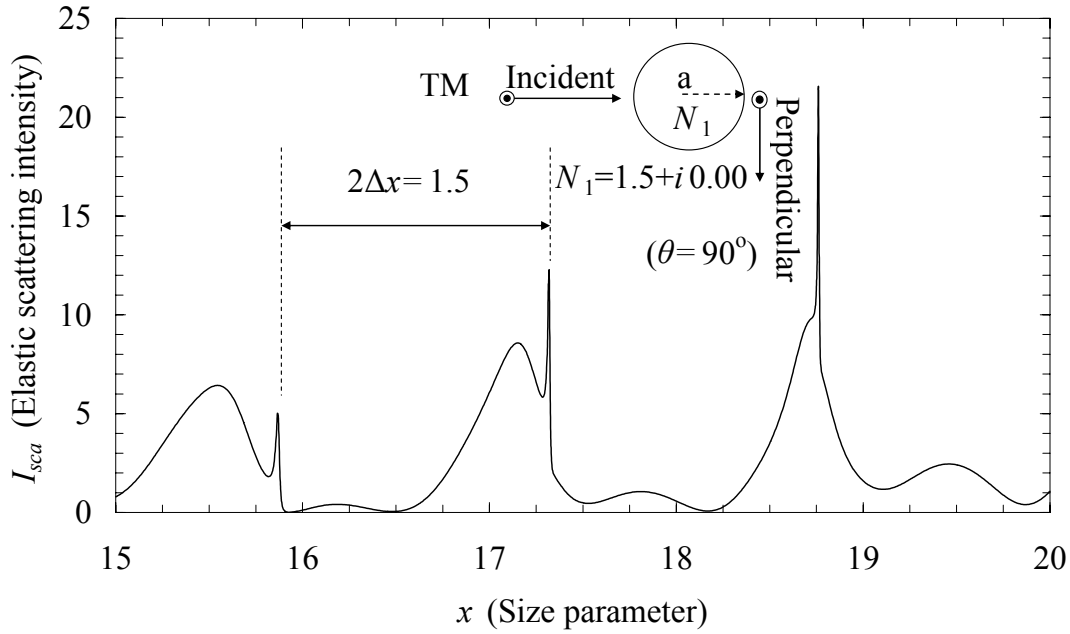

Figure 3.7: TM Perpendicular scattering intensity for a transparent silica cylinder.

In figure 3.7, the elastic scattering at 90° for TM polarization is shown. Due to the scattering angle of 90°, there is no background, so the total scattering intensity is less intense, however the MDR's are more clear. The MDR peaks are narrower. Noticeably, the number of resonances for perpendicular (90°) scattering is half the number of the resonances for forward scattering (0°). This difference is the result of the scattering angle of 90°. For forward (0°) and backward (180°) scattering, both even and odd resonant modes are observable, however, for perpendicular (90°) scattering only the even resonances can be observed, since the odd mode argument disappears at 90° [11, 67]. Therefore the mode spacing between the two consecutive modes with same mode order is twice of the calculated value of 0.75 at 90°.

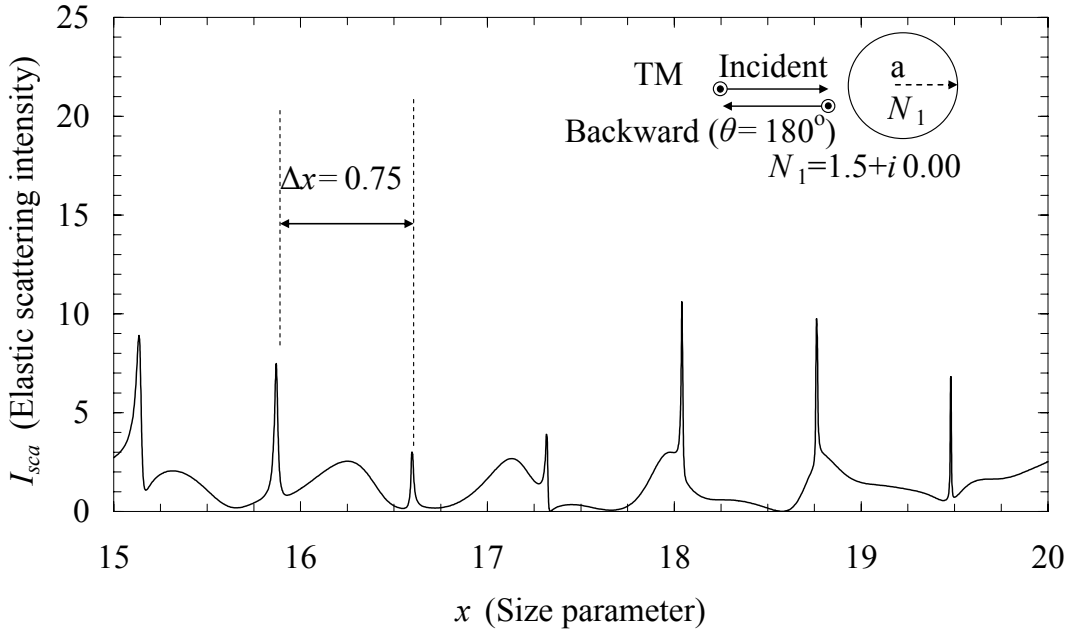

Figure 3.8: TM backward scattering intensity for transparent silica cylinder.

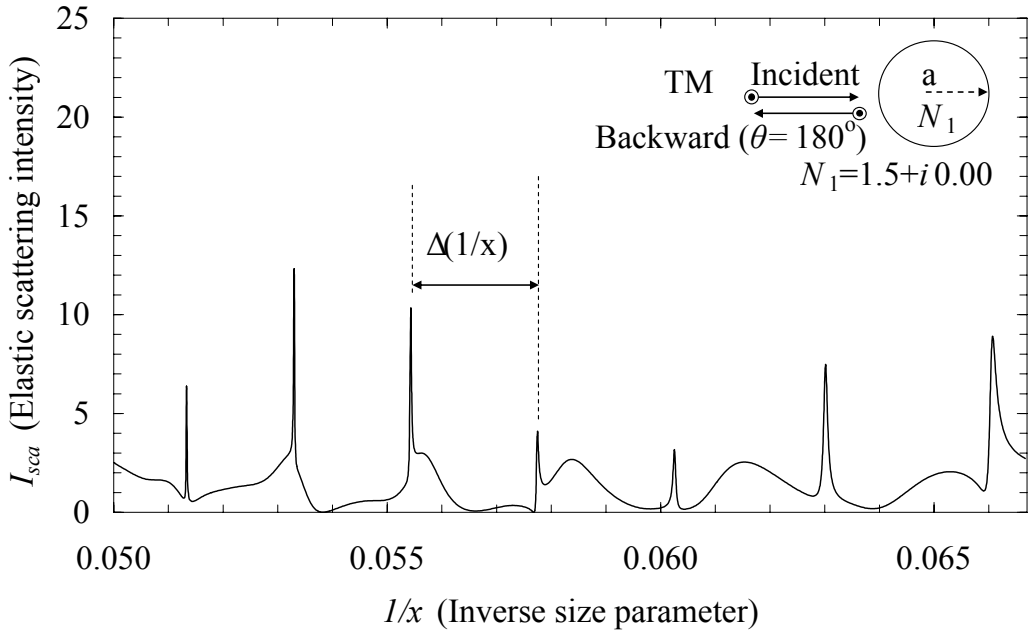

Figure 3.9: TM backward scattering intensity for transparent silica vs. 1/x.

In figures 3.8 and 3.9, the elastic scattering intensities are simulated for a scattering angle of 180°. In figure 3.8, the backward elastic scattering intensity is plotted as a function of size parameter, while in figure 3.9 the backward elastic scattering intensity is plotted as a function of the inverse size parameter, which is proportional to the wavelength. The number of resonances at 180° is the same with the number of resonances at 0°. The mode spacing is also found to be 0.75.

3.3. Silicon Microcylinder

The simulations similar to the silica cylinder are also performed for silicon cylinder. The real part of the refractive index of silicon is 3.5. The efficiencies for absorption, scattering and extinction are computed with a complex refractive index of 3.5+*i*0.05. Scattering, absorption and extinction efficiencies of a silicon cylinder for TM polarization are simulated and plotted in figure 3.10. The refractive index of the silicon cylinder is 3.5+*i*0.05, while the radius is *a*.

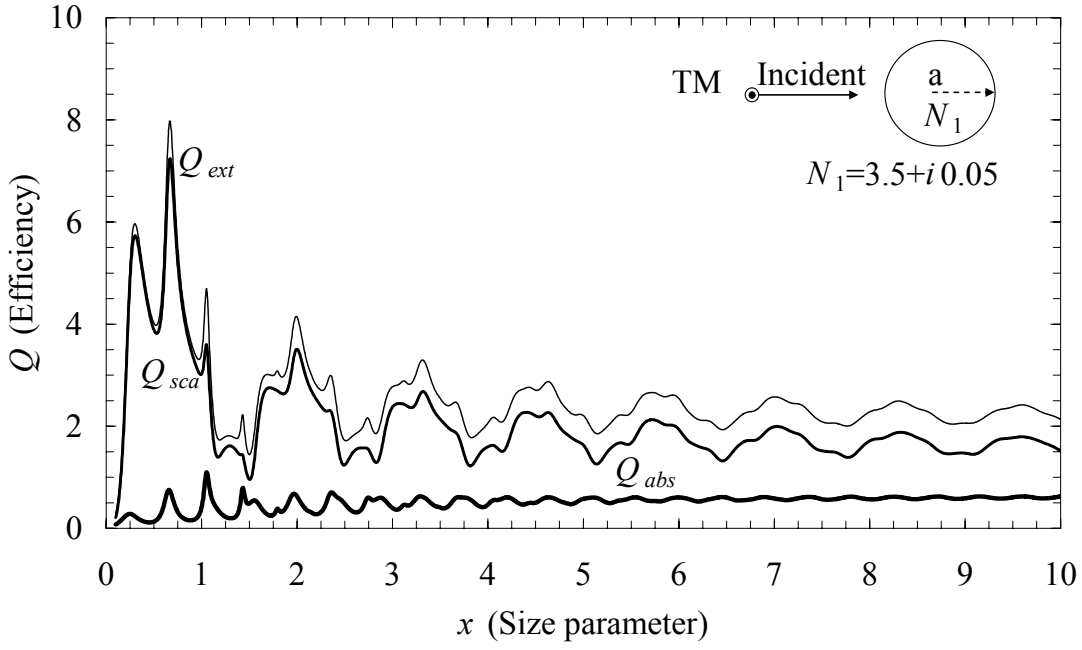

Figure 3.10: Extinction, scattering and absorption efficiencies for silicon cylinder.

As expected the absorption efficiency increases with increasing size parameter, while the scattering and extinction scattering efficiencies tend to decrease with increasing size parameter. Due to the increase in refractive index, the number of peaks increases in comparison to the silica cylinder, although oscillation behavior and the limiting efficiency value of 2.0 for extinction coefficient of the silicon cylinder are similar to the efficiency curve of the silica cylinder.

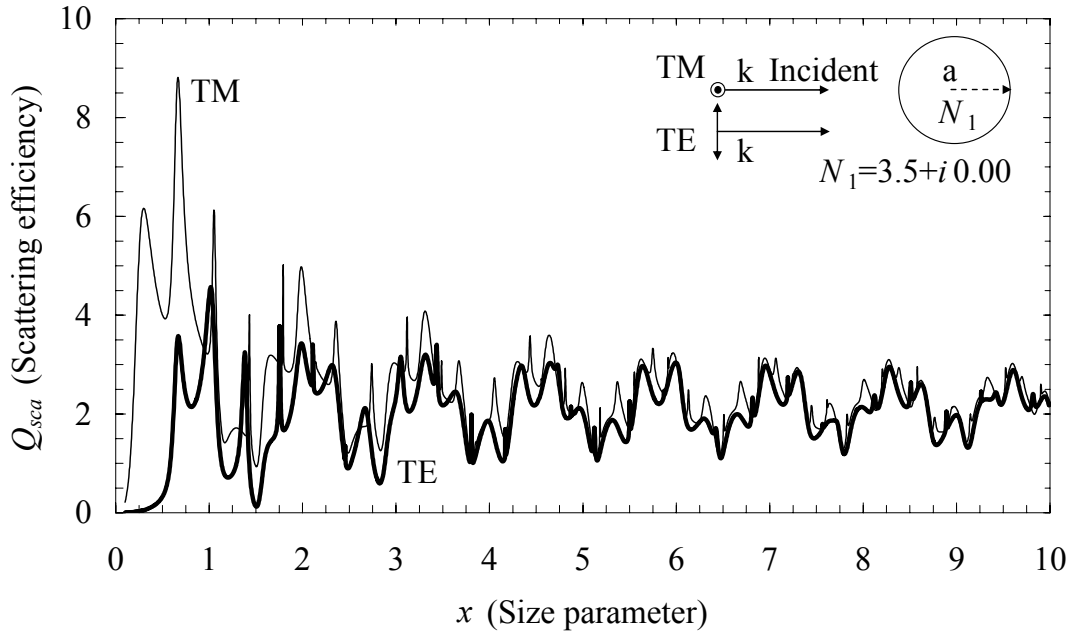

Figure 3.11: Scattering efficiencies for a transparent silicon cylinder.

Two simulations are performed for scattering efficiencies for both TE and TM polarizations. The refractive index is chosen to be 3.5 and the radius is a. The results are compared in figure 3.11. There is a difference between the TM and TE polarizations due to the polarization dependency of the scattering cross section; however the trends are same for both polarizations. Scattering efficiency decreases with increasing size parameter, and again the scattering efficiency tends to a limiting value of 2.0.

The scattering efficiency for TM polarization is simulated for size parameters between 15 and 20, and plotted in figure 3.12. As can be seen the limiting value of 2 is valid in also bigger size parameters. The resonant modes can be observed in the scattering efficiency curve.

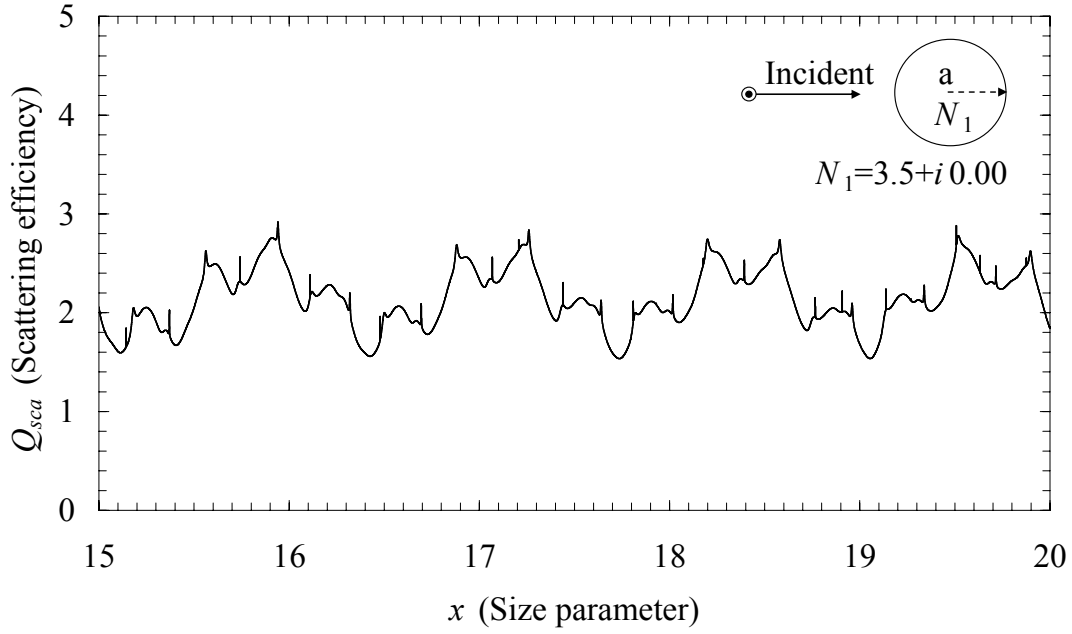

Figure 3.12: TM scattering efficiency for a transparent silicon cylinder.

The scattering intensities for different scattering angles of 0^o, 90^o and 180^o are simulated and plotted in figures 3.13, 3.14, 3.15, and 3.16. Similar to the silica simulation for forward scattering intensity, the intensity of the forward scattering for silicon cylinder has background intensity due to the incident plane wave. Also the mode spacing Δx is calculated as 0.38, and the simulation result is in agreement with the calculations. Higher order modes can also be observed in the scattering spectra.

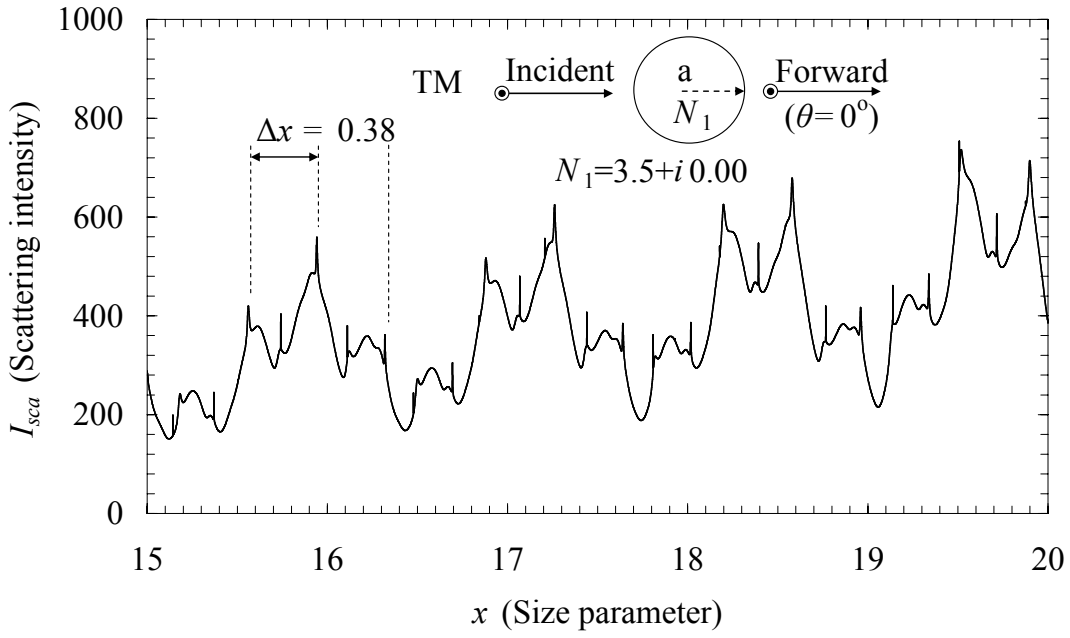

Figure 3.13: TM forward scattering intensity for a transparent silicon cylinder.

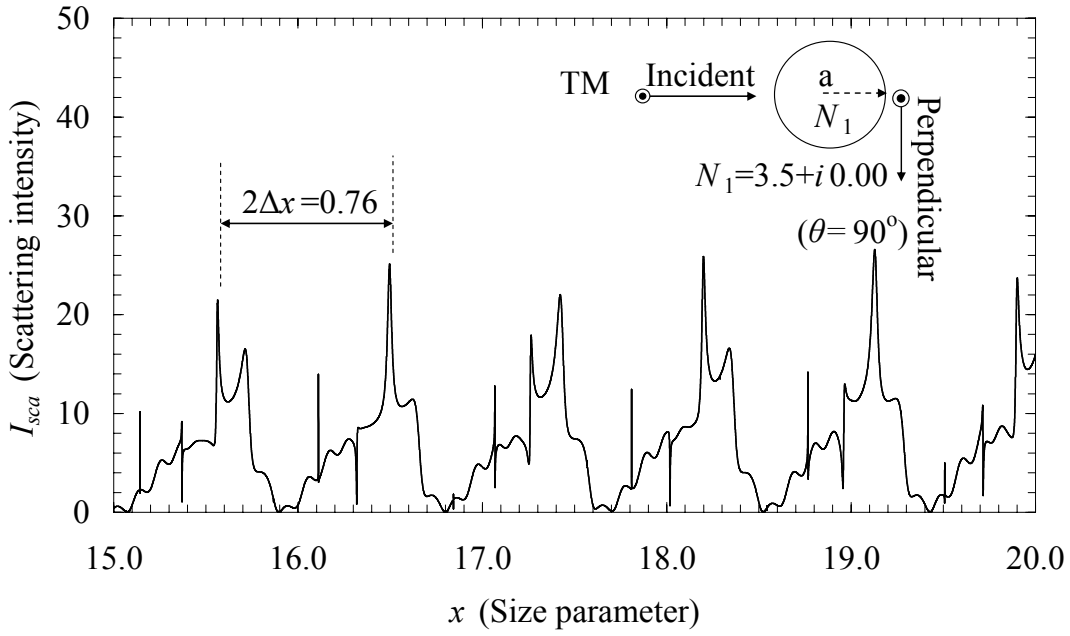

Figure 3.14: TM perpendicular scattering intensity for a silicon cylinder.

Elastic scatterings at 90° and 180° don't have a background; therefore the resonances are clearly identifiable with a bigger MDR-to-background ratio. Also, as expected, only even modes are observed for perpendicular scattering. Due to the elimination of the odd modes, the mode spacing is doubled for perpendicular scattering.

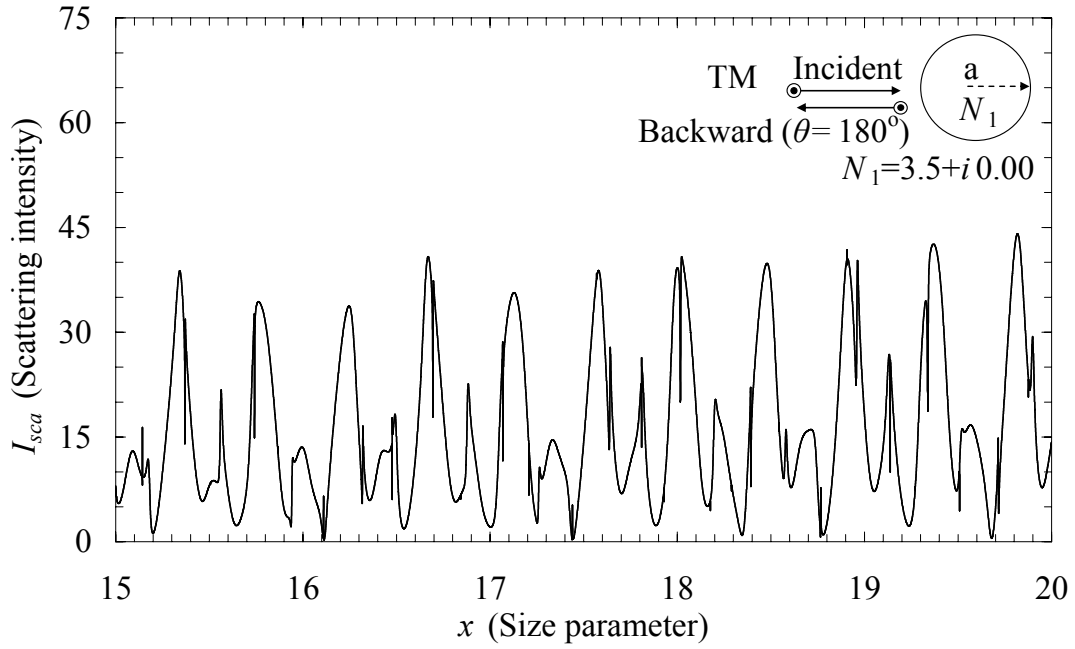

Figure 3.15: TM Backward scattering intensity for a transparent silicon cylinder.

In this chapter, efficiency factors for both silica and silicon cylinders are investigated. The oscillations structures are similar, and the limiting values for extinction coefficients are the same for both silica and silicon cylinders. However due to the dependency on the refractive index, efficiency curves show differences. These efficiency factor curves and the difference between them are in good agreement with the previous findings by van de Hulst [7], Bohren and Huffman [8], Barber and Hill [11], and Grandy [13]. After the interference structure, the scattering efficiency oscillates with increasing size parameter with a minimum limiting value of 2.0. The silicon cylindrical microresonator has more resonant modes than the silica resonator. Also the scattering light intensity from the silicon cylindrical microresonator is higher

than the scattering light intensity form the silica cylindrical microresonator, again due to the higher refractive index of silicon.

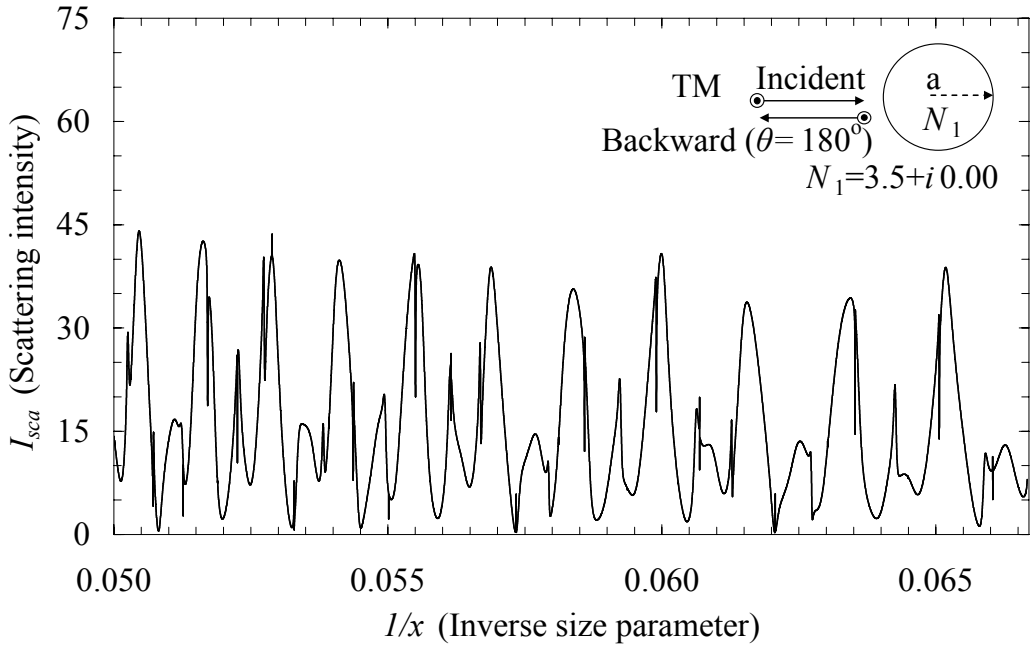

Figure 3.16: TM backward scattering intensity for a silicon cylinder vs. 1/x.

Chapter 4

SPHERICAL MICRORESONATORS

Due to their high quality factors and symmetrical morphology [16, 20], spherical microresonators (microspheres) are much more preferable than the other geometries. Therefore they are being used in various applications such as; light sources [22, 23], optical filters [33-35, 37, 38], optical modulators [42], and detectors [45-48] and photonic integration [57, 58, 67]. Microspheres can be regarded as 3-dimensionel resonators, and they can be used in photonic integrated circuits [68].

The resonance condition for the spheres is similar to the resonance condition for the cylinder. In addition, due to the spherical symmetry, efficiency factors are independent of the polarization of the light.

4.1. Spherical Resonator

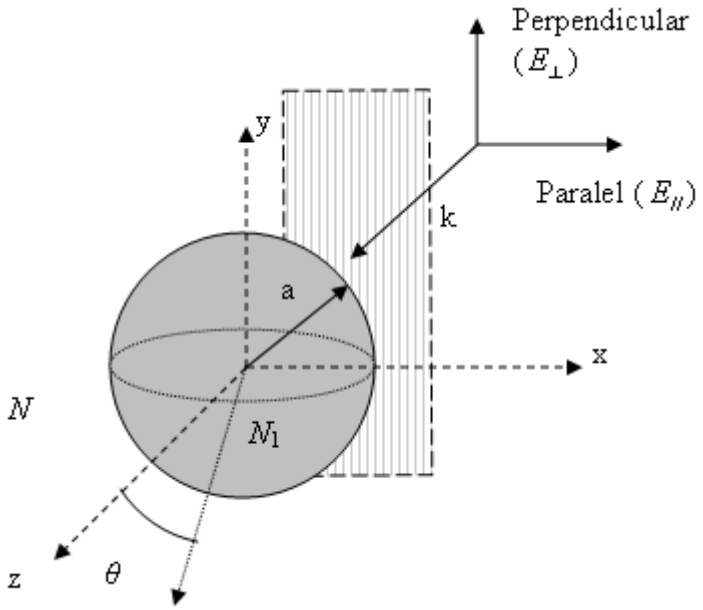

Figure 4.1: Spherical resonator configuration.

The spherical resonator model that is used for calculations is illustrated in figure 4.1. The radius of the sphere is *a*. The spherical microresonator is illuminated with an incident plane wave. The polarizations are defined as parallel and perpendicular to the scattering plane (*z*-*x* plane). Scattering efficiencies and scattering light intensities for different angles from both silica and silicon microspheres are calculated.

Mode spacing between the two consecutive resonances with the same mode order of a spherical resonator is [65]:

$$\Delta x = \frac{x\left[\arctan\left(\sqrt{\left(\frac{Mx}{n}\right)^2 - 1}\right)\right]}{n\left(\sqrt{\left(\frac{Mx}{n}\right)^2 - 1}\right)} \qquad (4.1).$$

If, *x*/n is approximately 1.0, the mode spacing can also be found by the following simplified equation [65].

$$\Delta x = \frac{\arctan\sqrt{M^2 - 1}}{\sqrt{M^2 - 1}} \qquad (4.2).$$

4.2. Silica Microsphere

A silica microsphere with a refractive index of 1.5+*i*0.01 is chosen as a spherical microresonator to perform the simulations for efficiency factors, and scattering intensities for different angles.

The efficiency factors for silica spherical microresonator are shown in figure 4.2. The scattering efficiency of a silica spherical resonator with a size parameter range between 15 and 20 is plotted in figure 4.3.

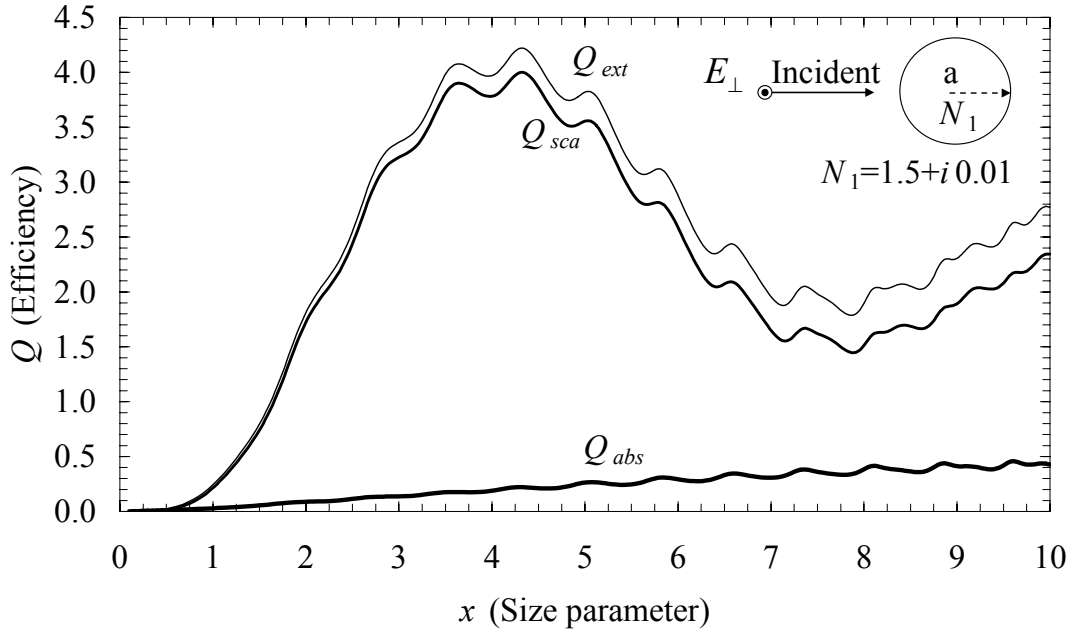

Figure 4.2: Extinction, scattering, and absorption efficiencies for a silica sphere.

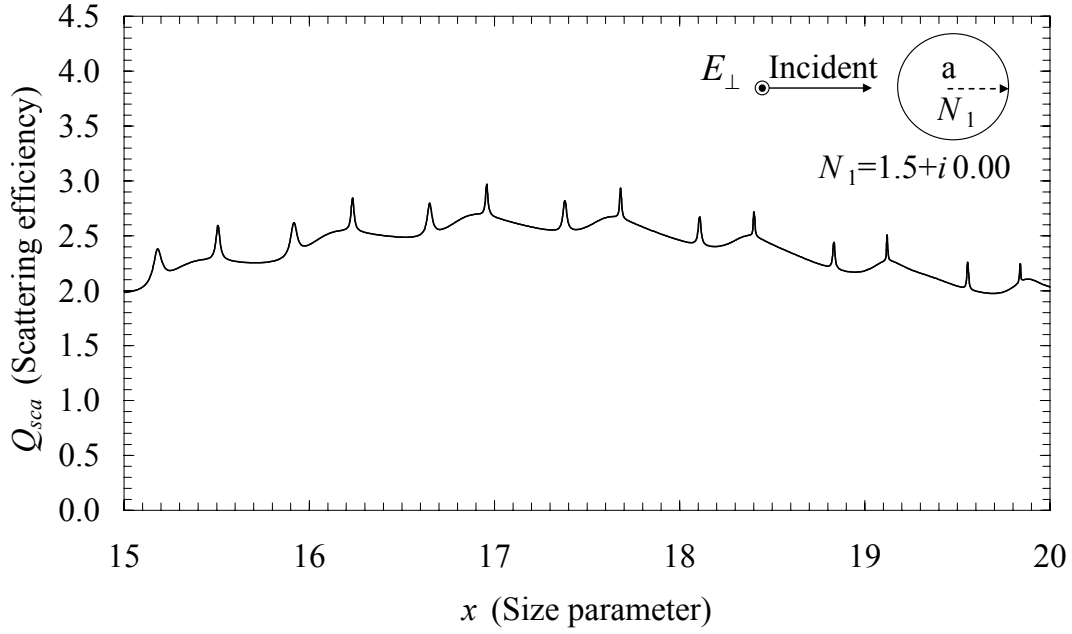

Figure 4.3: The scattering efficiency for a silica sphere.

The ripple structure and the interference oscillation are observed as in figure 4.2. As explained in the previous chapter, the ripple structure represents the morphology dependent resonances (MDR's). The oscillation above the limiting value of 2.0 represents the interference of the incident (transmitted) plane wave, and the scattered (diffracted) wave, while the limiting value is caused by the doubled scattering cross section due to the both geometric and diffraction contributions.

Scattering light intensities for forward scattering (θ=0^o) (Figure 4.4), perpendicular scattering (θ=90^o) (Figure 4.5), and backward scattering (θ=180^o) (Figure 4.6) are calculated for a silica microsphere. The backward scattering intensity for silica spherical microresonator is also plotted as a function of inverse size parameter, i.e., proportional to the wavelength.

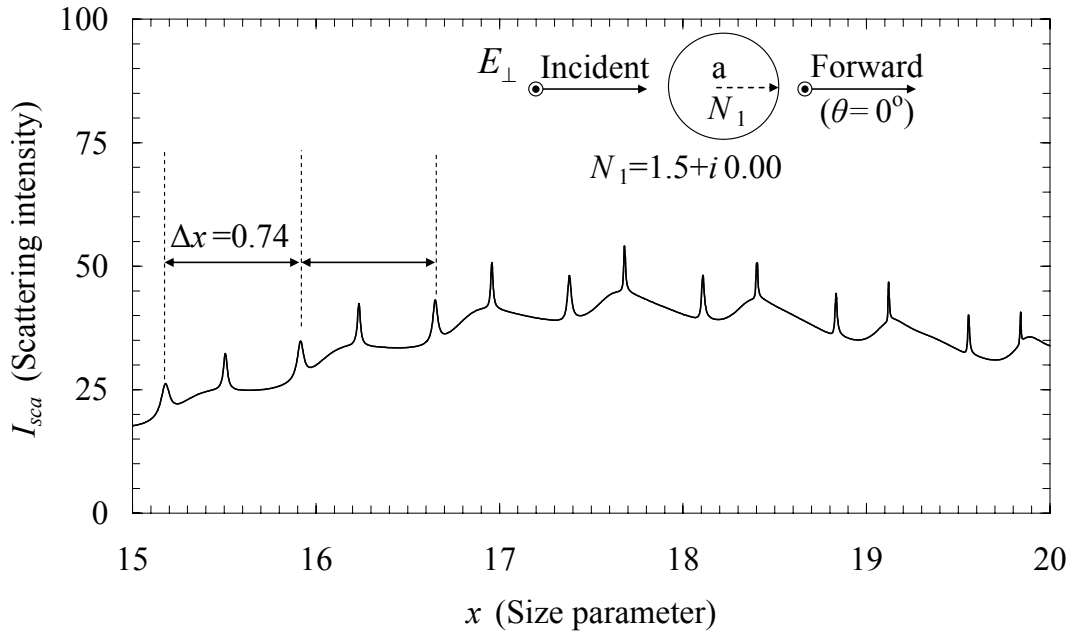

Figure 4.4: Forward scattering intensity (Perpendicular) for silica sphere.

Since, the forward scattering is in the direction of the incident wave, the forward scattering is observed with a background in figure 4.4. The mode spacing between the consecutive modes with the same mode order is calculated as 0.75 by using the mode spacing equation. The calculated value is in agreement with the mode

spacing of the simulated resonances which is 0.74. Also higher order modes are observable on the figure 4.4 between the consecutive resonant modes.

In figure 4.5, the scattering light intensity from the silica sphere at θ=90^o is plotted. The direction of the scattered light is perpendicular to the direction of the incident light, therefore scattering spectrum is cleared out from the background intensity and the MDR-to-noise ratio is increased. Also, due to the elimination of the odd mode numbers, only the even modes can be observed in the perpendicular scattering spectrum, and therefore the mode spacing is twice of the calculated mode spacing.

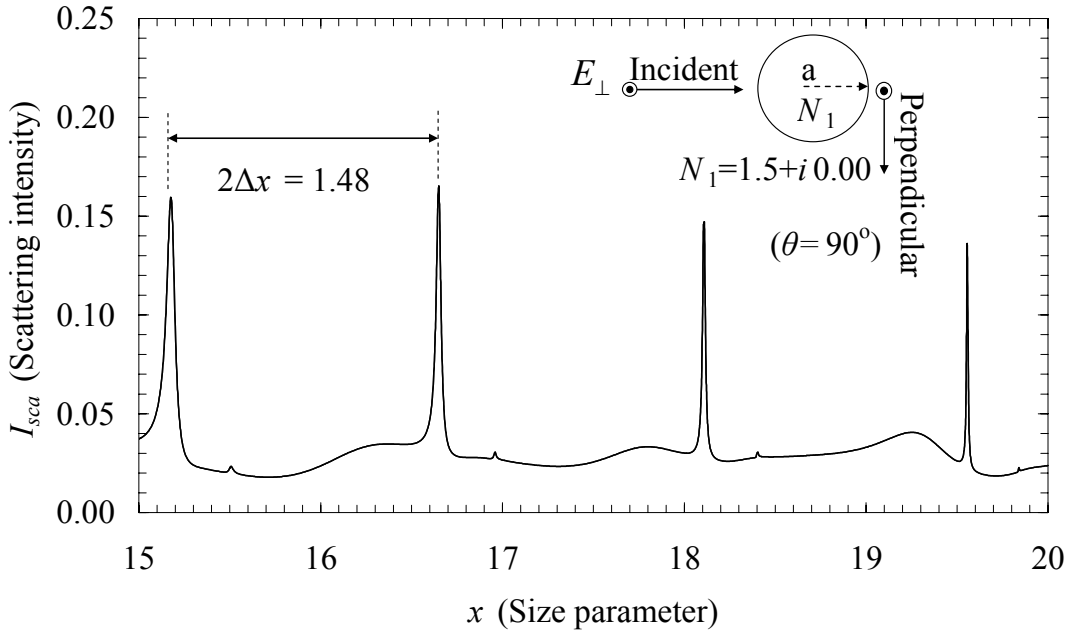

Figure 4.5: Perpendicular scattering intensity (Perpendicular) for silica sphere.

In figures 4.6, and 4.7, the backward scattering spectrum is plotted against size parameter and inverse size parameter. As expected, the odd numbers are restored in the scattering spectra. There is no background due to the incident light. However, in comparison to the perpendicular light scattering, the backward scattering intensity is high, since $\pm\theta$ are degenerate at the 180^o.

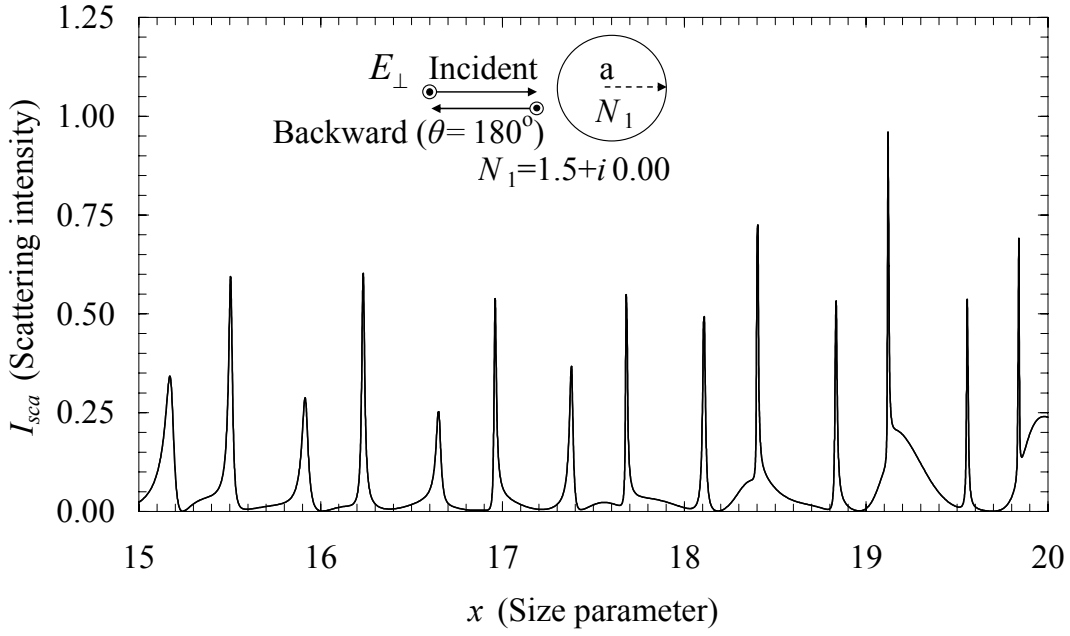

Figure 4.6: Backward scattering intensity (Perpendicular) for silica sphere.

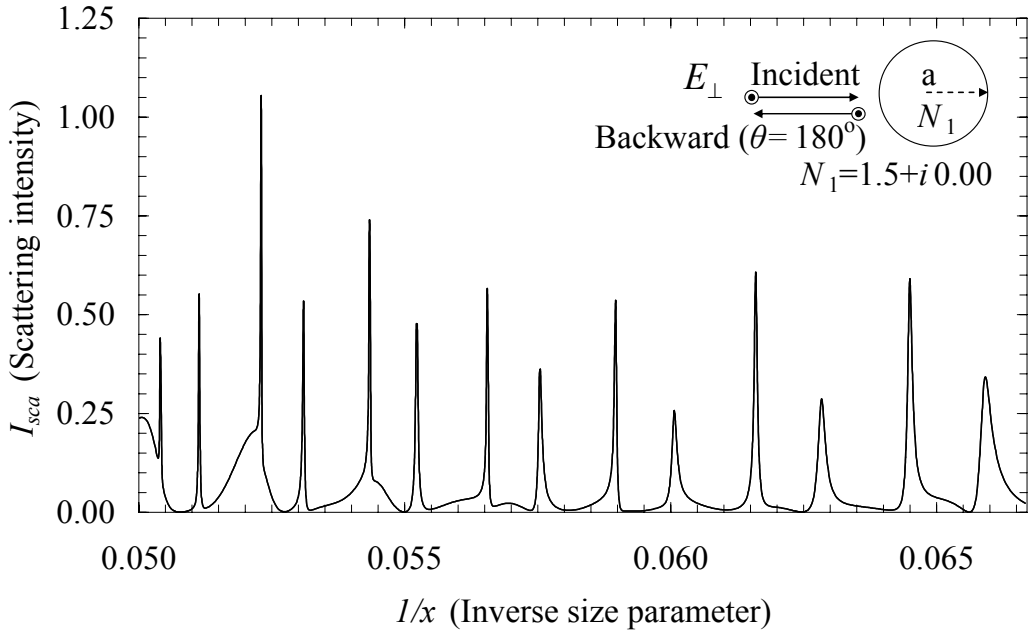

Figure 4.7: Backward scattering intensity (Perpendicular) for silica sphere vs. 1/x.

4.3. Silicon Microsphere

Simulations are also performed for silicon microsphere with a refractive index of 3.5+*i*0.05. The complex refractive index is used for calculating the scattering, absorption and extinction efficiencies (Figure 4.8).

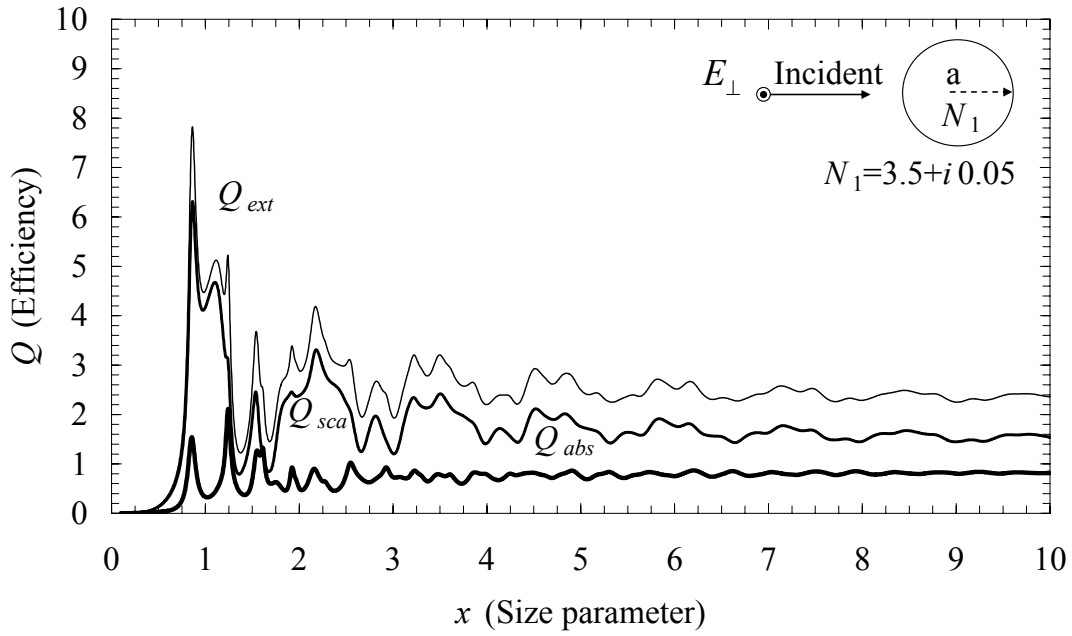

Figure 4.8: Extinction, scattering, and absorption efficiencies for a silicon sphere.

As expected, the number of modes in silicon is higher than the number of modes in silica, since, the refractive index of silicon is higher than silica. Oscillation behavior due to the interference is still observable. The oscillation is attenuated and goes to the limiting value of 2.0 as the size parameter increases. This limit is also shown in the following figure.

Elastic scattering efficiency is plotted in figure 4.9 for a refractive index of 3.5 and radius of *a*. As size parameter varies between 15 and 20, the scattering efficiency is oscillating around the value of 2.

For light illumination with perpendicular polarization, the forward scattering, perpendicular scattering, and backward scattering are also calculated and presented in the following figures.

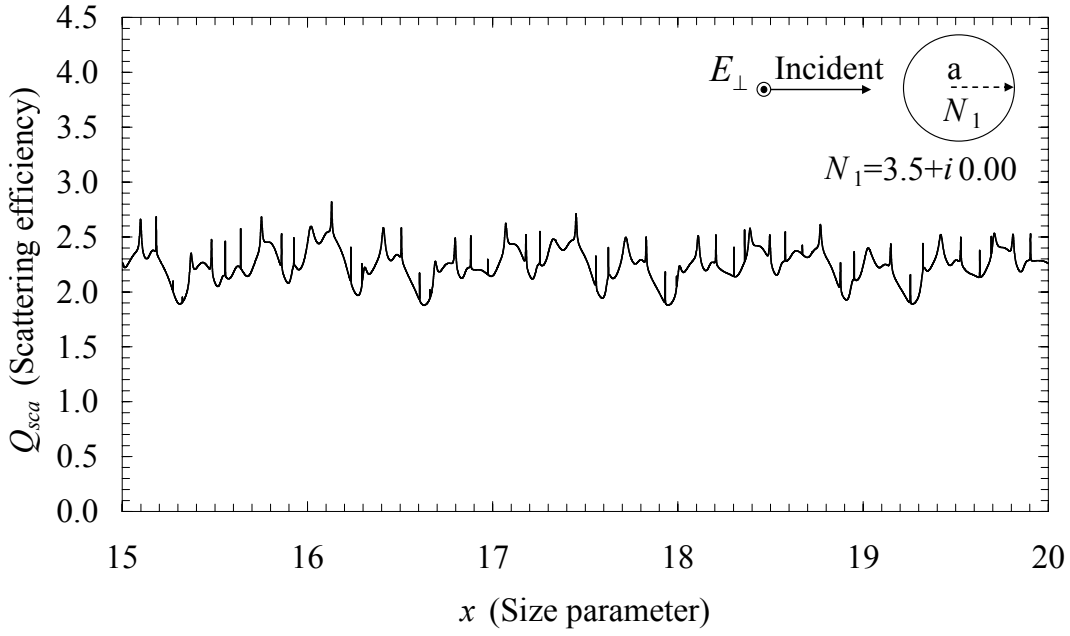

Figure 4.9: Scattering efficiency for a transparent silicon sphere.

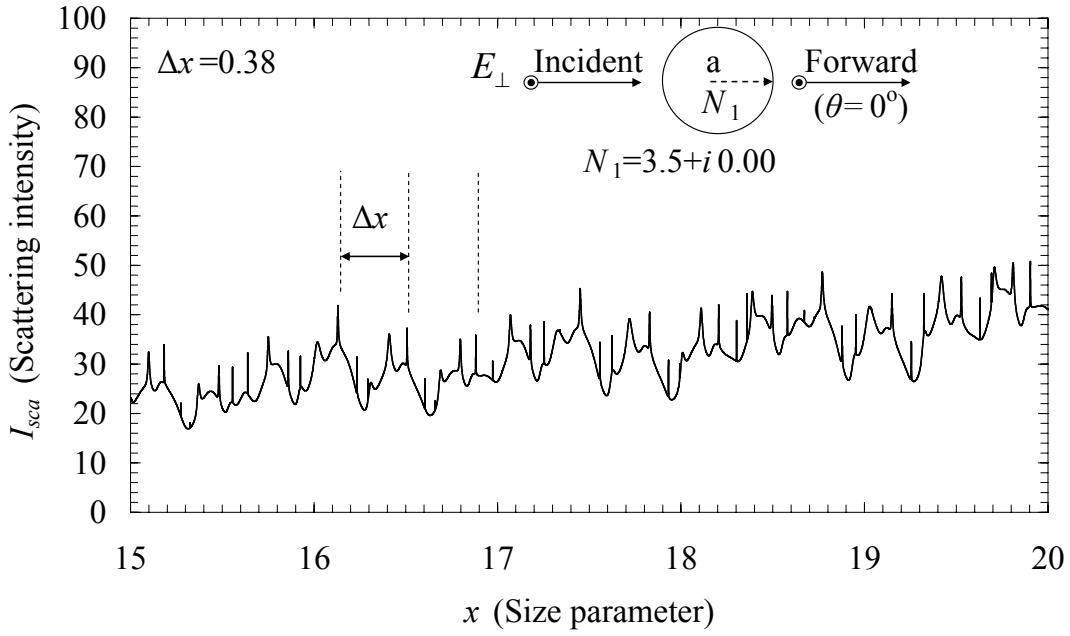

Figure 4.10: Forward scattering intensity (perpendicular) for a silicon sphere.

In figure 4.10, the forward elastic scattering for a transparent silicon sphere (θ=0^o) is shown. The peaks represent the resonances, and the background intensity due to the incident light intensity. In figure 4.11, the perpendicular elastic scattering (θ=90^o) is shown. The scattering light intensity has minimum background. The number resonance is half of the number of resonances when compared with the forward elastic scattering as expected. Mode spacing is twice of the calculated value.

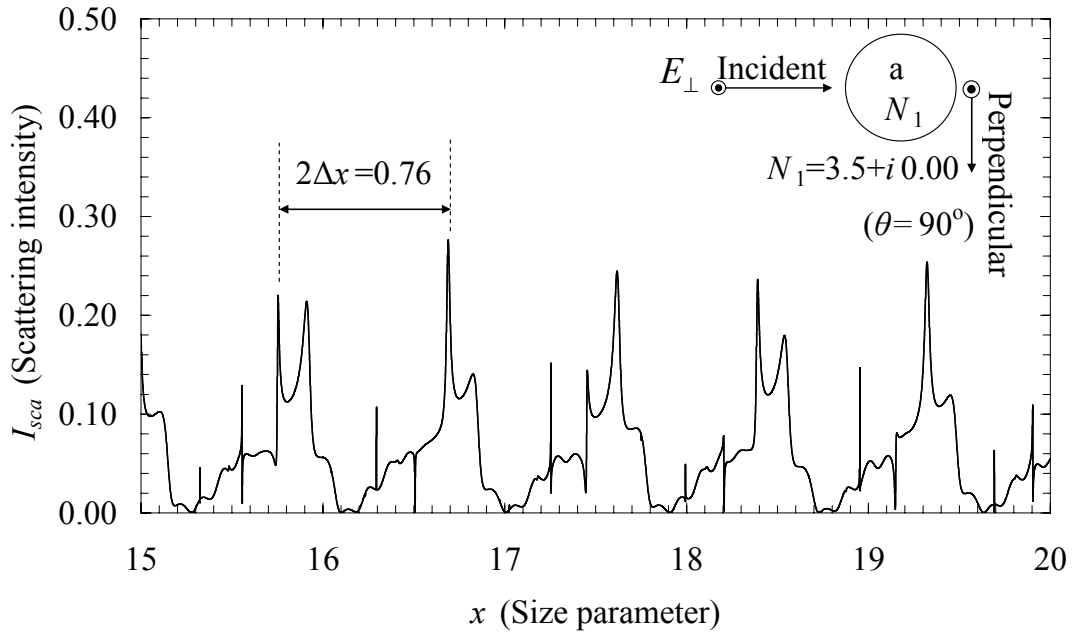

Figure 4.11: Perpendicular scattering intensity for a transparent silicon sphere.

Backward scattering light intensity with respect to the size parameter and the inverse size parameter are plotted in figures 4.12 and 4.13, respectively. Spectra include high order modes.

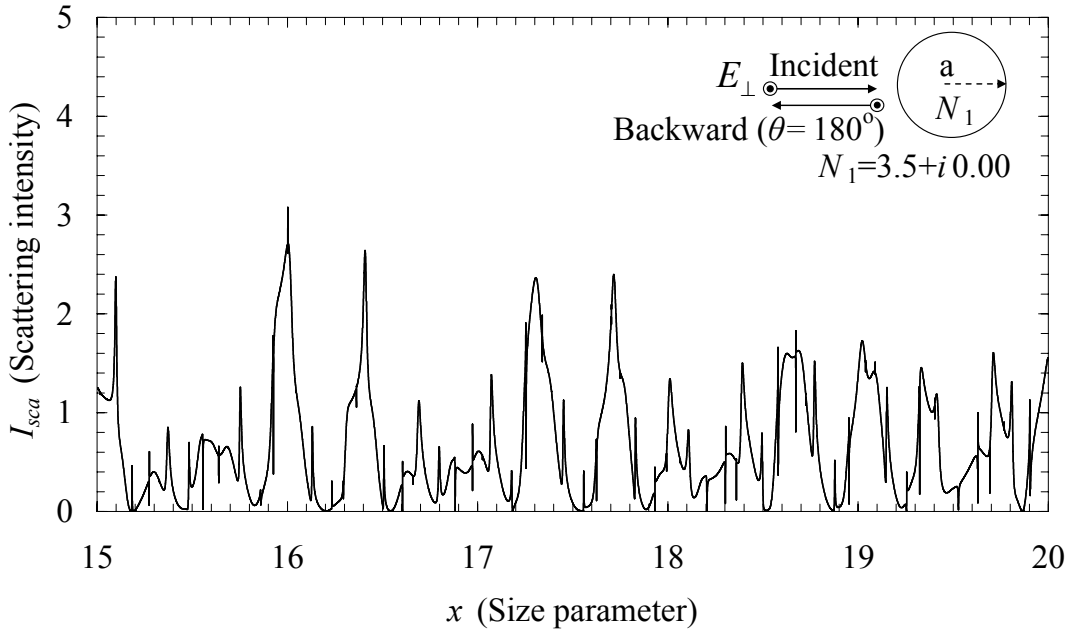

Figure 4.12: Backward scattering intensity (perpendicular) for a silicon sphere.

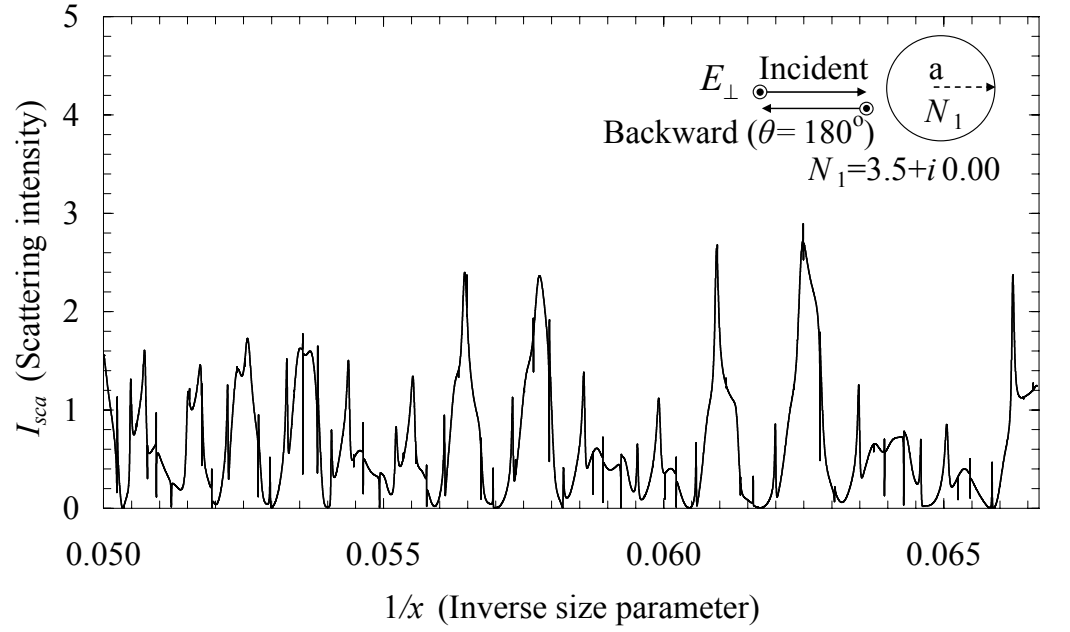

Figure 4.13: Backward scattering intensity for a silicon sphere vs. 1/x.

4.4. Elastic Light Scattering from a Silicon Sphere

In order to compare the simulation results, and to provide a comparison with experimental data, the following setup is used. Plane wave is used to illuminate the resonators in our simulations, while Gaussian beam is used in the experimental setup. The solutions for plane wave, and Gaussian beam are different, however, the elastic scattering at 90° is similar, due to the absence of the background.

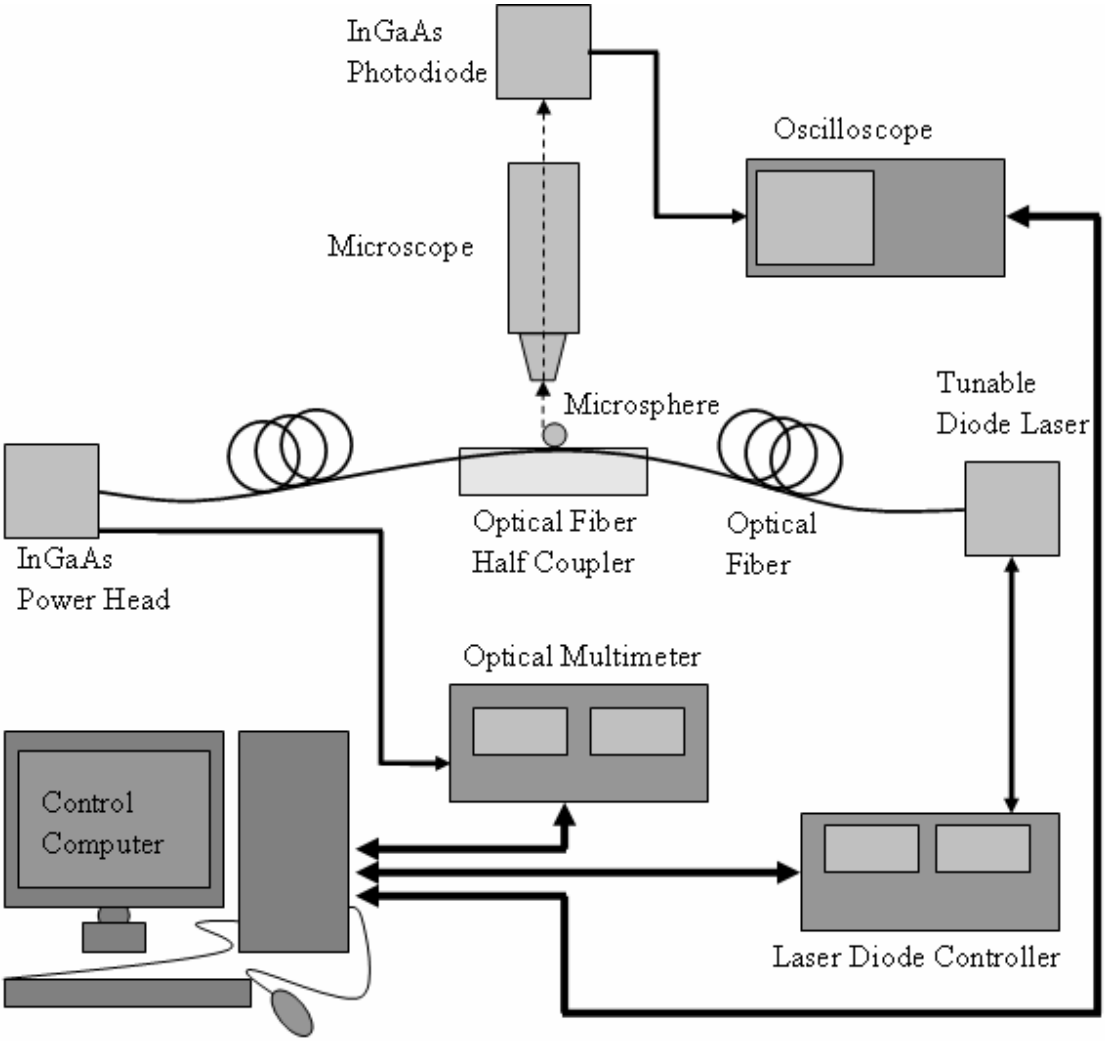

Figure 4.14: Experimental setup for elastic light scattering from silicon spheres.

A tunable diode laser (1473 nm) is driven by a laser diode controller, which is controlled by a computer. The lasing wavelength of the diode laser is controlled via a

computer, and the laser beam is sent to the optical fiber, which is connected to the optical fiber half coupler (OFHC). On the top of the OFHC, there is a silicon sphere with a refractive index of 3.5, and a radius of approximately 500 microns. A microscope is arranged in such a way, that it collects scattered light from the sphere at 90^{o}. Scattered light passes through the microscope and is incident on the InGaAs photodetector. InGaAs photodetector is connected to the oscilloscope and the computer is connected to the oscilloscope via a GPIB interface. The computer is also used to collect data from the optical multimeter, which is connected to the InGaAs power head for the transmitted light.

The perpendicular scattering light intensity from the silicon sphere is plotted by using experimental data. The mode spacing between the two consecutive modes with the same mode order can be also written as a function of wavelength [58] as:

$$\Delta\lambda = \frac{\lambda^2 \arctan\sqrt{M^2 - 1}}{2\pi a N \sqrt{M^2 - 1}} \qquad (4.1),$$

where M is the relative refractive index ratio, a is the radius of the sphere, and λ is the wavelength of light in the vacuum, and N is the refractive index of the surrounding medium.

In figure 4.5, the mode spacing for silicon sphere with a radius of 500 microns is found to be 0.27 nm for wavelength of 1474 nm. This experimental value is in good agreement with the calculated mode spacing of 0.26 nm. Due to the large size of the sphere, the elastic scattering spectrum contains many resonant modes.

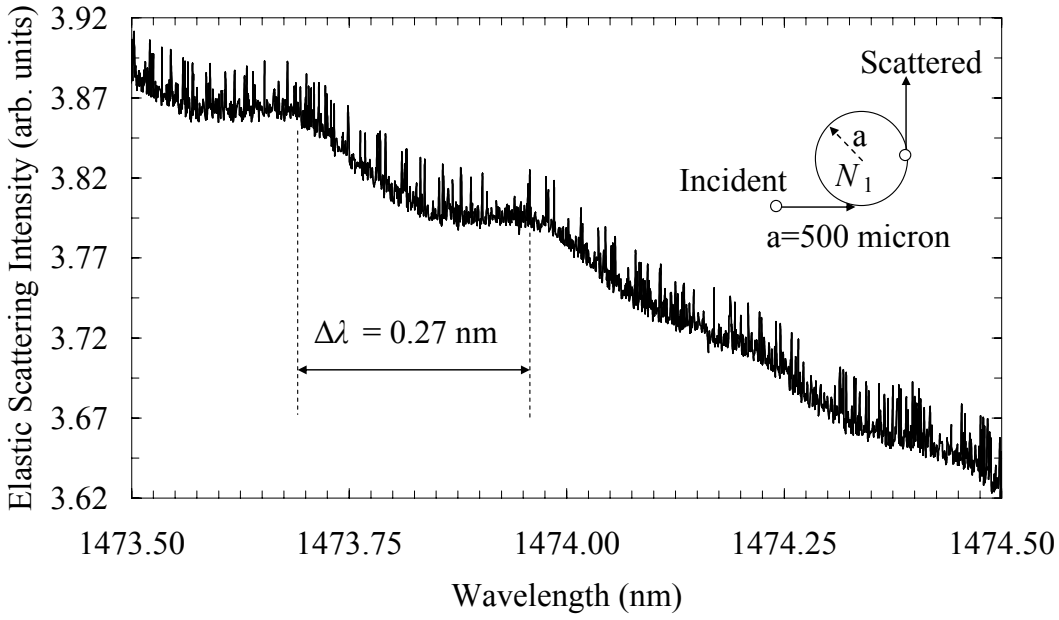

Figure 4.15: TE polarized elastic scattering from the silicon sphere.

Chapter 5

SPHEROID MICRORESONATORS

Spheroids are interesting geometrical shapes, and the light scattering from spheroids is worth investigating. Multiple studies are performed on deformed spheres and spheroid resonators and their resonant modes [69-72].

5.1. Spheroid Resonator

There are two types of spheroids (oblate, and prolate). We will cover only the prolate in this chapter.

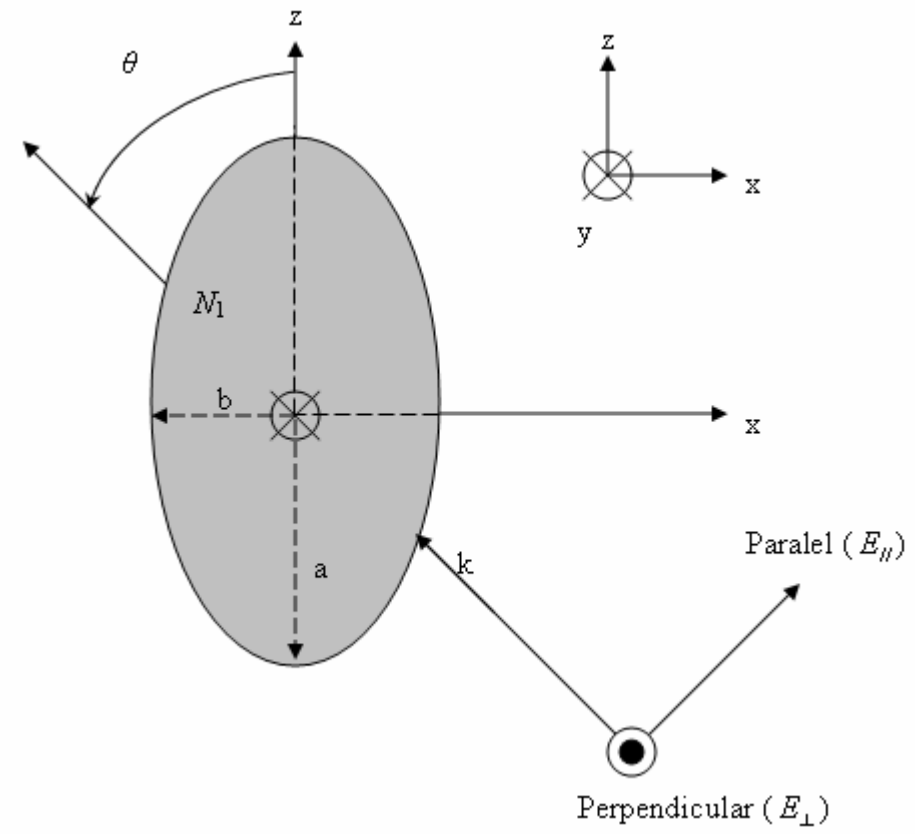

Figure 5.1: Prolate resonator excitation configuration.

In figure 5.1, a prolate and an incident plane wave are illustrated. The equivalent size parameter of a prolate (a>b) spheroid is defined as:

$$x_{spheroid} = x_{sphere} \times (a/b)^{2/3} \quad (5.1),$$

where *a/b* is called as the axial ratio of a spheroid [11]. This equivalent size parameter is defined for an equivalent sphere with a same volume as the prolate.

The scattering efficiency calculations with respect to size parameter are performed for silica, silicon nitride, and silicon materials with a refractive index of 1.5, 2.0, and 3.5, respectively.

5.2. Silica Microspheroid

Simulations for transparent silica microspheroids are performed and results of these calculations are plotted in figures 5.2, 5.3, 5.4, and 5.5.

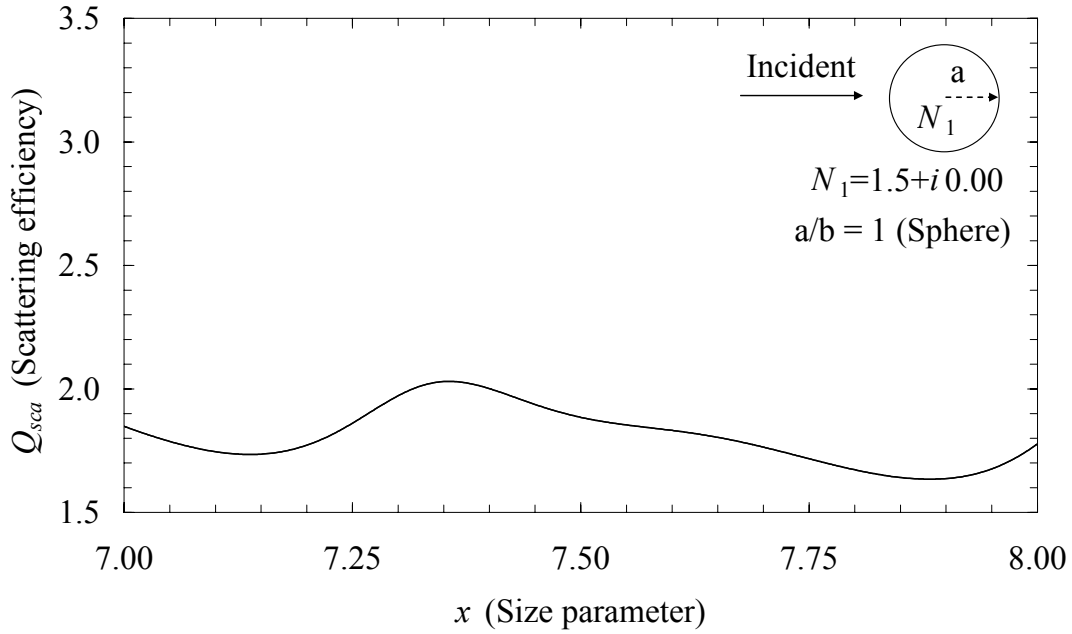

Figure 5.2: Scattering efficiency for a transparent silica sphere.

In figure 5.2, scattering efficiency from a silica sphere is shown. Due to the low refractive index, the scattering efficiency spectrum does not show any high-Q resonance peaks. The same situation is also observed in figures 5.3, 5.4, and 5.5, which the scattering efficiencies for parallel polarization, perpendicular polarization, and random orientation are shown, respectively.

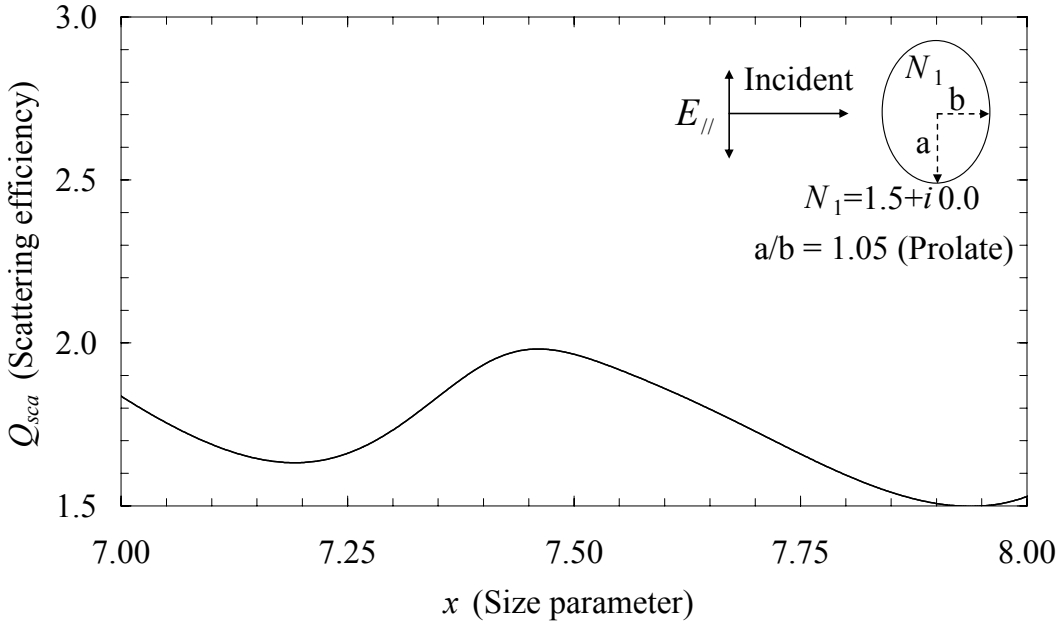

Figure 5.3: Scattering efficiency (parallel polarization) for silica prolate.

As can be seen from the figures 5.3 and 5.4, the scattering efficiencies for perpendicular and parallel polarizations differ as spherical shape deforms to a spheroid. As the deformation continues, the geometry of the prolate tends to a cylinder, and the scattering efficiencies for the prolate tend to the scattering efficiencies for a cylinder for respective polarizations. In figure 5.5, the calculation for random orientation is performed.

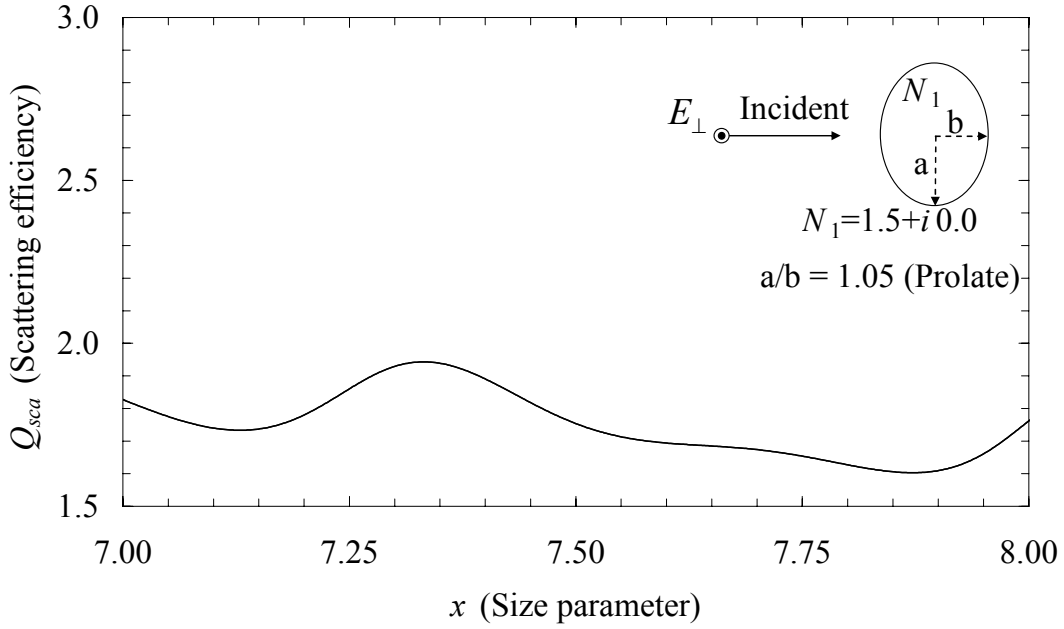

Figure 5.4: Scattering efficiency (perpendicular polarization) for silica prolate.

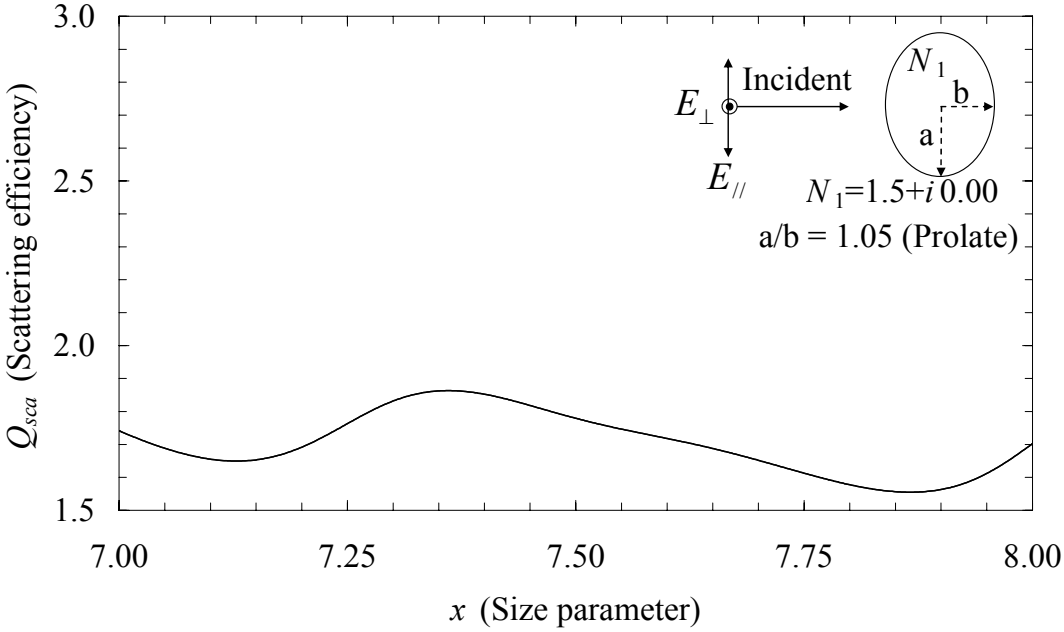

Figure 5.5: Scattering efficiency (random orientation) for silica prolate.

5.3. Silicon Nitride Microspheroid

The silicon nitride with a refractive index of 2.0 is used for following calculations. In figure 5.6, the scattering efficiency for a silicon nitride sphere is plotted. High-Q resonance peaks are observed for the silicon nitride sphere. In addition to the polarization dependency of a spheroid, another property for spheroids is observed in figures 5.7, and 5.8. When sphere is deformed to a spheroid with an axial ratio of 1.05, degenerate resonance peaks split. The splitting increases as the axial ratio increases.

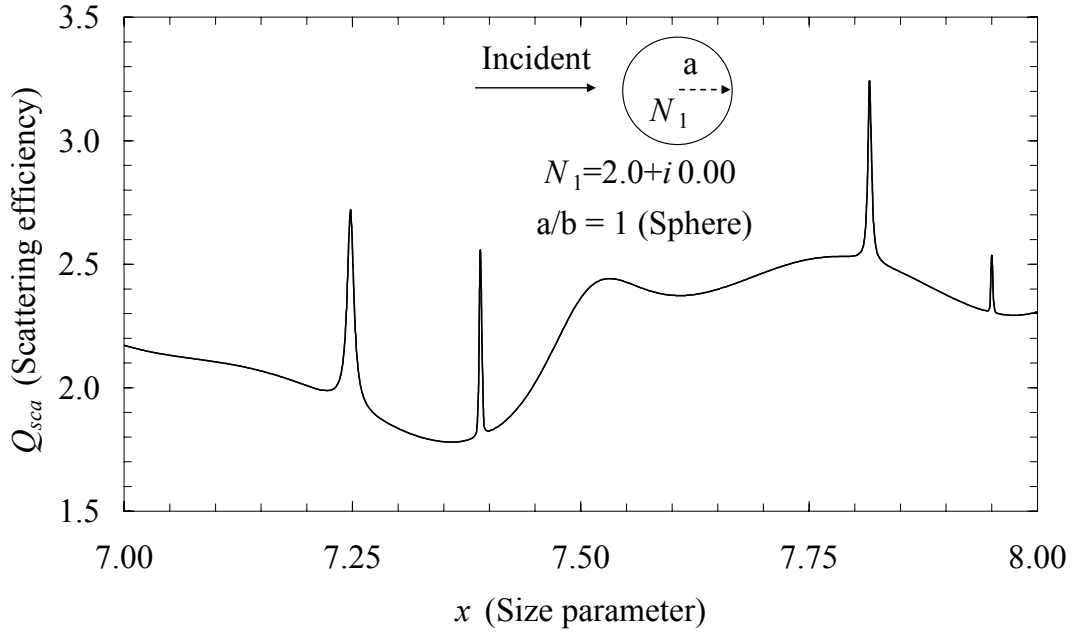

Figure 5.6: Scattering efficiency for a silicon nitride sphere.

As can be seen from figures 5.7, and 5.8, the degenerate modes are splitting with deforming the shape of the sphere. Therefore, scattering spectra for a spheroid includes those non-degenerate modes. The mode splitting for a spheroid with an axial ratio of 1.05 is found to be 1.1% of the original mode for spherical resonator of the same material.

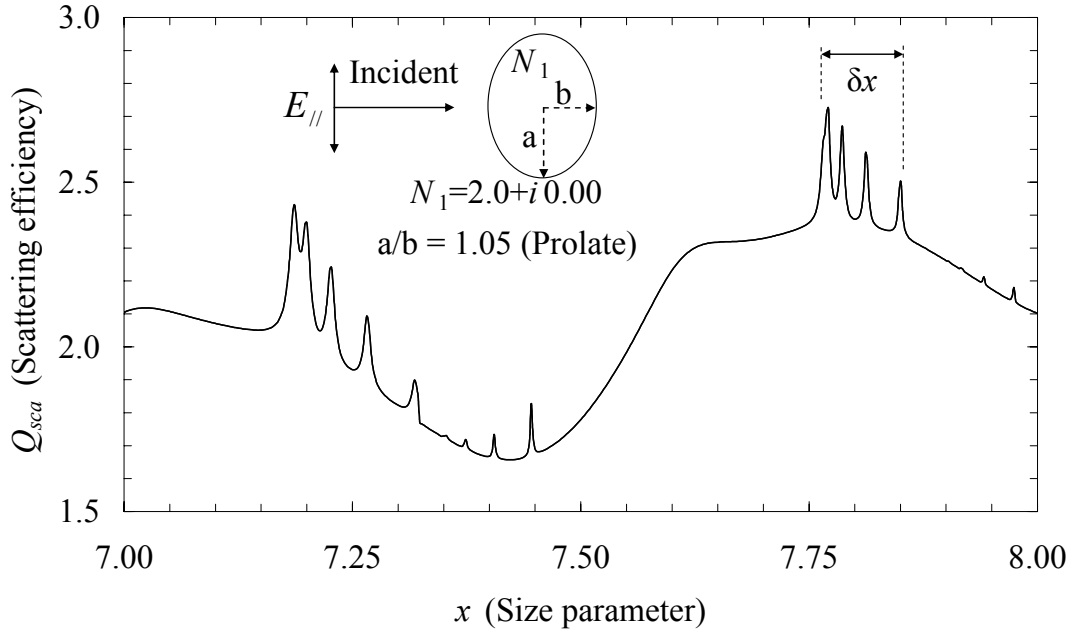

Figure 5.7: Scattering efficiency (parallel) for silicon nitride prolate.

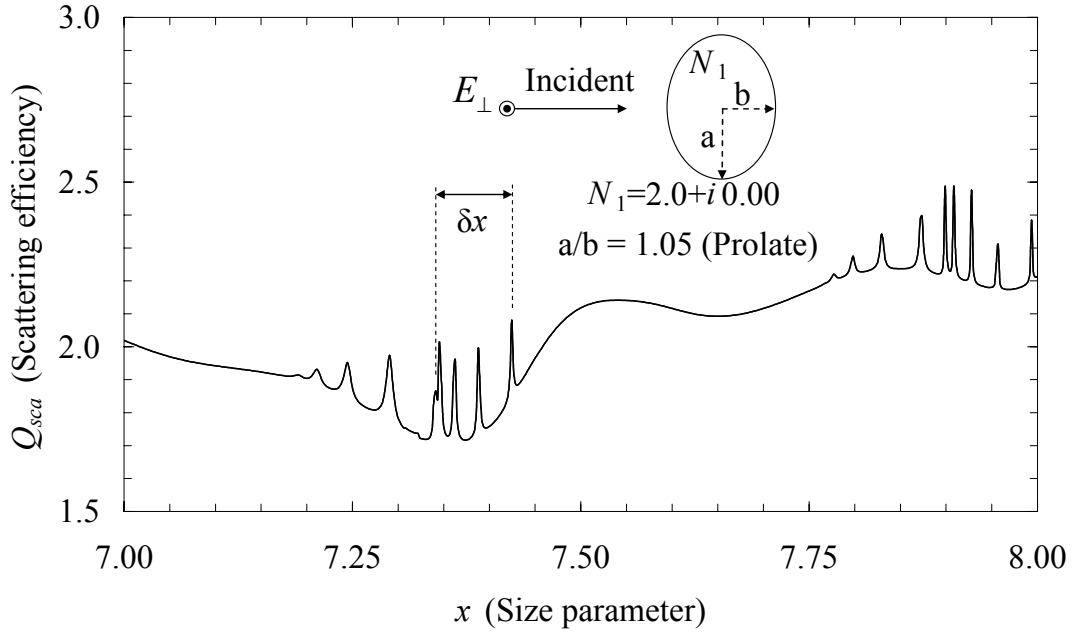

Figure 5.8: Scattering efficiency (perpendicular) for silicon nitride prolate.

The mode splitting is defined as:

$$\frac{\delta w(m)}{w_o} = 1 - \frac{e}{6}\left(\frac{3m^2}{n(n+1)}\right) \tag{5.2},$$

where, $\delta w(m)$ is the mode splitting in angular frequency, n the mode number, w_o the frequency of the n^{th} mode, m the azimuthal mode number, and e the morphology distortion [71, 72]. The distortion is defined as [71, 72]:

$$e \equiv \frac{a-b}{a_{sphere}} \tag{5.3}.$$

Mode splitting for a silicon nitride prolate with an axial ratio of 1.05 is calculated to be 1.5% by using equation 5.2 and it is in good agreement with the calculations.

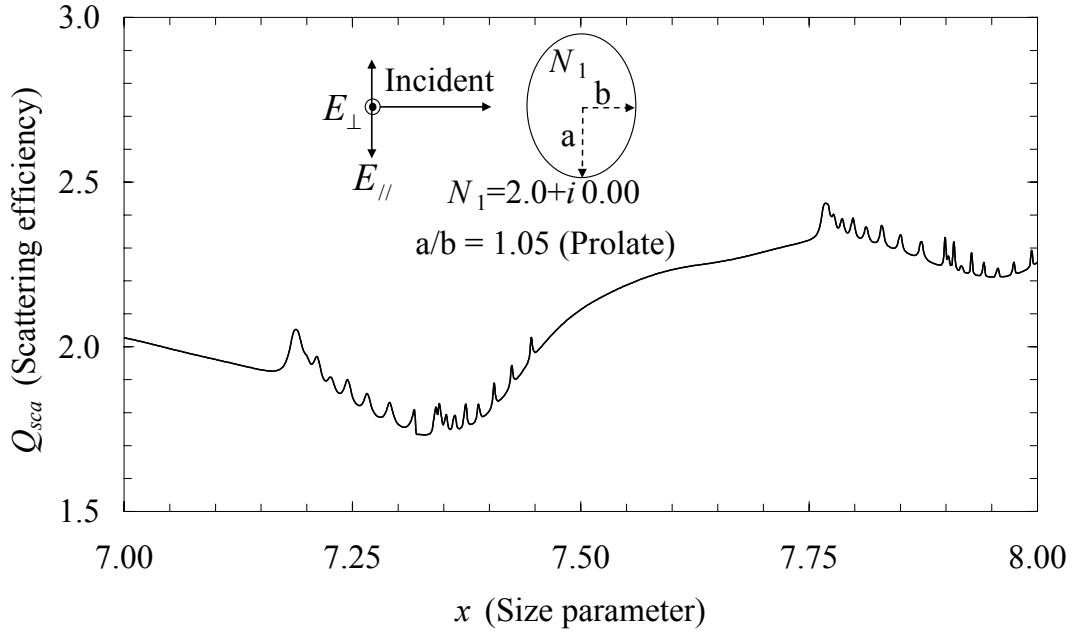

Figure 5.9: Scattering efficiency (random) for silicon nitride prolate.

5.4. Silicon Microspheroid

Calculations for silicon spheroids are also performed. In figure 5.10, the scattering efficiency for a silicon sphere is calculated. In figures 5.11 and 5.12 the scattering efficiencies of a silicon spheroid with an axial ratio of 1.05 are calculated for different polarizations, while in figure 5.13, the calculation is performed for random orientation.

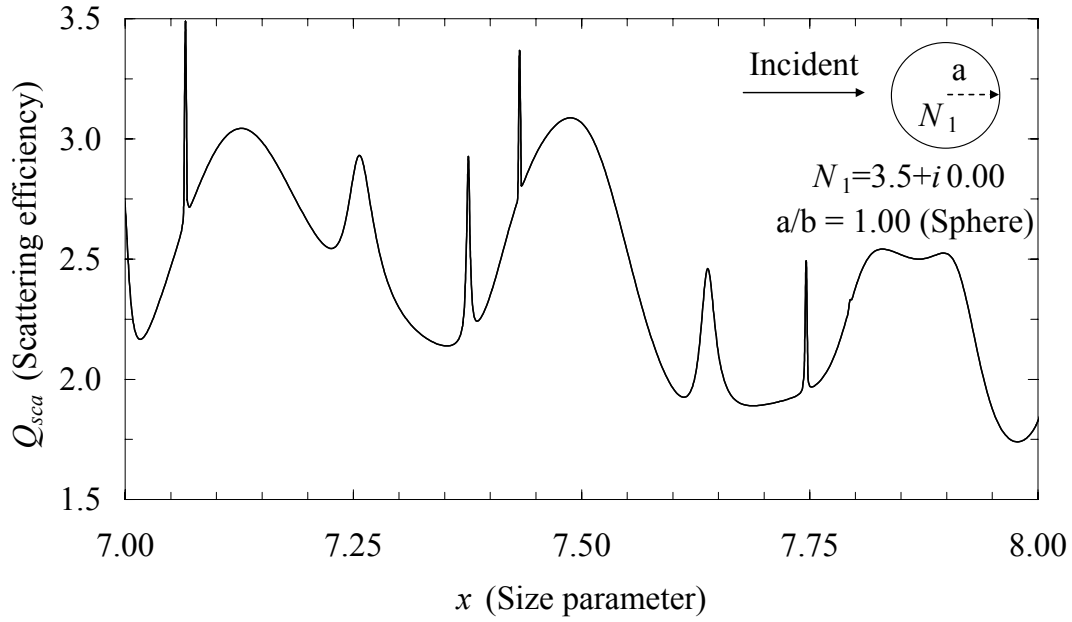

Figure 5.10: Scattering efficiency for a silicon sphere.

As can be seen on figures, the resonant peaks, that are observed for silicon spherical resonator (in figure 5.10), split into degenerate modes with the geometrical deformation of the microsphere (figures 5.11 and 5.12). As the polarization dependency is introduced again to the scattering efficiency, the perpendicular and the parallel scattering efficiencies are different for spheroids. By using equation 5.2, the mode splitting is calculated as 0.3 %, while the simulation is resulted with a mode splitting of 0.4% for silicon prolate with an axial ratio of 1.05.

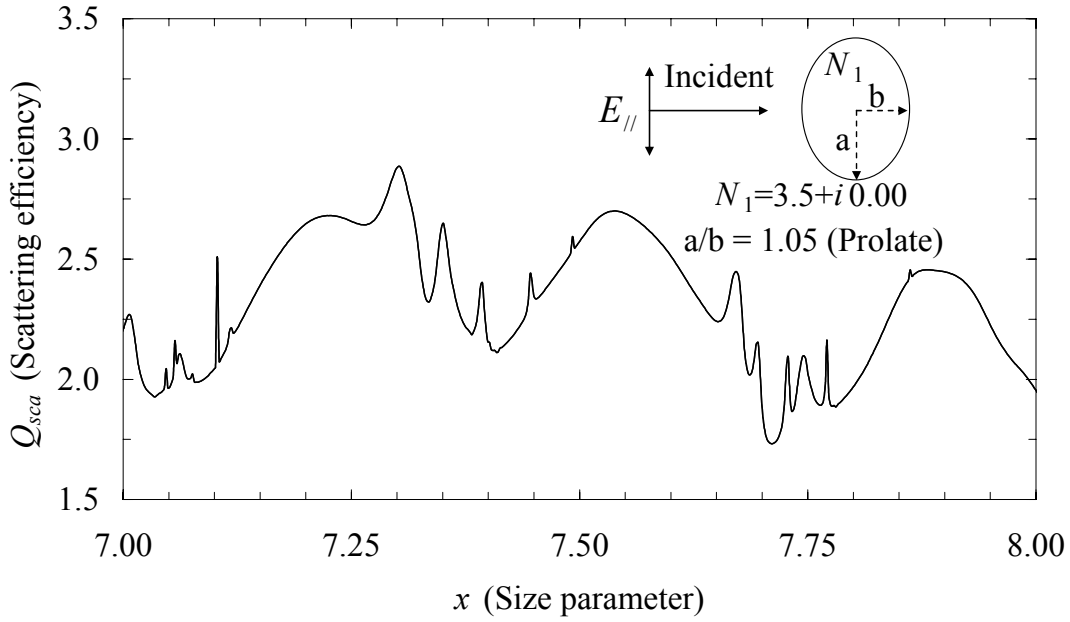

Figure 5.11: Scattering efficiency (parallel polarization) for silicon prolate.

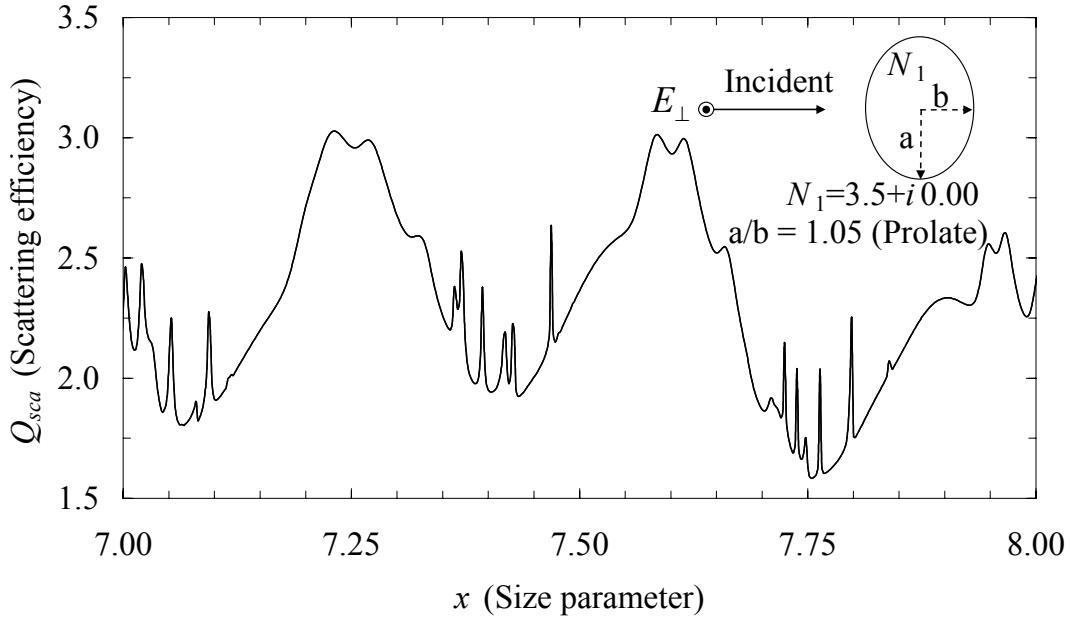

Figure 5.12: Scattering efficiency (perpendicular polarization) for silicon prolate.

In the following figure, the scattering efficiency for random orientation is shown.

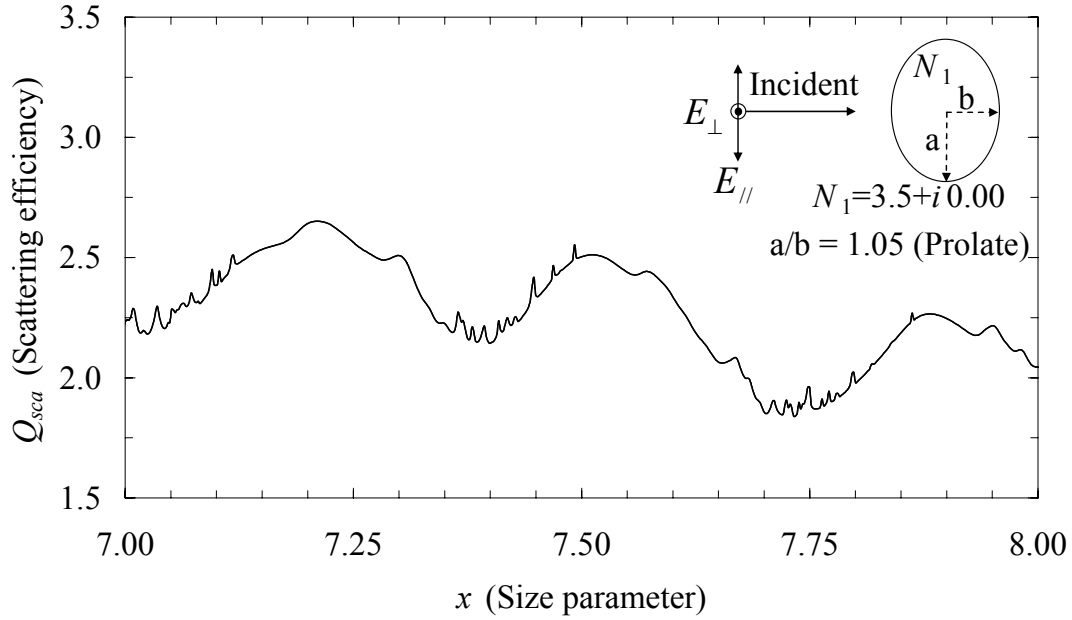

Figure 5.13: Scattering efficiency (random orientation) for silicon prolate.

As a result, the mode splitting for spherical deformation is observed for both silicon nitride, and silicon resonators. Moreover, mode splitting is not the only result of deformation. A shift in wavelength is also observed for spherical deformation [50, 70 and 72]. Therefore, by using mode separation, and mode shift, new photonic applications can be envisioned.

Chapter 6

CONCLUSION

In this work, the morphology dependent resonances were calculated, and studied in the elastic scattering spectra of microparticles for potential applications in silica and silicon photonics. The elastic scattering from silica, silicon microresonators with different morphologies were investigated with numerical simulations. An experimental elastic scattering spectrum for a silicon spherical resonator is provided for comparison with the simulation results.

In chapter 1, the slab microresonators were studied, and the resonances were observed for silica and silicon. In chapter 2, the elastic light scattering from cylindrical microresonators is investigated. The scattering efficiencies of spherical resonators were calculated, and perpendicular light scattering intensity from the silicon sphere is experimentally shown in chapter 3. Spheroid resonators were simulated, and the scattering efficiencies for different polarizations were calculated for silica, silicon nitride, and silicon in chapter 4.

By simulating the slab resonator, simplest type of the resonators, the morphology dependent resonances were shown. These modes are result of a resonance condition for a resonator, which depends on the size and the refractive index of the resonator material. Due to this dependency, these resonances can only be accessed for certain size parameters, or wavelengths.

Simulations for silica and silicon cylindrical resonators were performed, and the extinction, scattering, and absorption efficiency factors were calculated. In addition to those efficiencies, scattering intensities were studied for three specific angles. The scattering efficiency has a limiting value of 2.0, due to the additional diffraction from the resonator. In addition to the limiting factor, the interference of incident and the scattered waves causes an oscillation structure. Spherical resonator simulations for silicon and silica were also performed and extinction, scattering, and

absorption efficiency factors were investigated as well as the scattering intensities for three specific angles.

Similar to cylindrical resonators, the scattering efficiency curve for spherical resonators have also the MDR ripples and oscillation structures, and again the limit value of 2.0. In the cylindrical and spherical resonators, the forward light scattering intensity has a high background intensity caused by the incident light. The elastic scattering light intensities at 90^o (perpendicular scattering) and 180^o (backward scattering) were observed to be free out of this background, and MDR-to-background ratios were higher. The perpendicular scattering spectra for cylindrical and spherical resonators have half of the modes as compared to the number of modes for forward and backward scattering. Finally, spheroid resonators of silica, silicon nitride and silicon were investigated. Mode splitting due to the deformation of the spherical morphology is observed.

In summary, by numerically simulating slab, cylinder, sphere, and spheroid geometries of silica, and silicon resonators, elastic light scattering from these resonators and resonant modes were studied, and analyzed. As a future work, scattering efficiencies for oblate spheroid resonators can be studied, and morphology dependent resonances for those resonators can be identified through the elastic light scattering spectra.

VITA

Ersin Hüseyinoğlu was born in Trabzon, Turkey in 1983. He attended elementary school in Iskenderpaşa Ilkokulu in Trabzon. Later, he graduated from Trabzon Kanuni Anadolu Lisesi in 2000. After graduation, he was accepted to Yeditepe University (in Istanbul) Physics program as an undergraduate student. While studying physics, he was also accepted to Electrical and Electronics Engineering program at the same university for double major study.

He worked with Prof. Dr. Rabia İnce, and received his B.Sc. degree in Physics after defending his B.Sc. thesis that covers his experimental work on optics. In 2008, he was accepted to Material Science and Engineering M.Sc. program at Koç University (in Istanbul) as a teaching and research assistant. He joined the Koç University Microphotonics Research Laboratory led by Prof. Dr. Ali Serpengüzel.

In 2009, he received his B.Sc. degree in Electrical and Electronics Engineering from Yeditepe University, after defending his B.Sc. thesis in that covers his theoretical work on optics with Dr. Cahit Canbay.

During his study in Koç University Microphotonics Research Laboratory, he worked on optical microresonators and their applications in optoelectronics and photonics.

Contact: e.huseyinoglu@ieee.org / ehuseyinoglu11@alm.ku.edu.tr

BIBLIOGRAPHY

1. L. Rayleigh, “The problem of the whispering gallery”, Scientific papers 5, 617 (1912).
2. A. Ashkin and J.M. Dziedzic, “Observation of resonances in the radiation pressure on dielectric spheres”, Phys. Rev. Lett. 38, 1351-1354 (1977).
3. A. Ashkin and J.M. Dziedzic, “Observation of optical resonances of dielectric spheres by light scattering”, Appl. Opt. 20, 1803-1814 (1981).
4. P. Chýlek, V. Ramaswamy, A. Ashkin and J. M. Dziedzic, “Simultaneous determination of refractive index and size of spherical dielectric particles from light scattering data”, Appl. Opt. 22, 2302-2307 (1983).
5. R.E. Benner, P.W. Barber, J.F. Owen and R.K. Chang, “Observation of structure resonances in the fluorescence spectra from microspheres”, Phys. Rev. Lett. 44, 475-478 (1980).
6. S.C. Hill, R.E. Benner, C.K. Rushforth and P.R. Conwell, “Observation of structure resonances in the fluorescence spectra from microspheres”, Phys. Rev. Lett. 44, 475-478 (1980).
7. H.C. van de Hulst, “Light Scattering by Small Particles”, Denver, New York (1981).
8. C.F. Bohren and D.R. Huffman, “Absorption and Scattering of Light by Small Particles”, Wiley-Interscience, New York (1983).
9. M. Kerker, “Selected Papers on Light Scattering”, SPIE, Washington (1983).
10. P.W. Barber and R.K. Chang, “Optical Effects Associated With Small Particles”, World Scientific, Singapore (1988).
11. P.W. Barber and S.C. Hill, “Light Scattering by Particles: Computational Methods”, World Scientific, Singapore (1990).
12. R.K. Chang and A.J. Campillo, “Optical Processes in Microcavities”, World Scientific, Singapore (1996).

13. W. T. Grandy, Jr., “Scattering of Waves from Large Spheres”, Cambridge University Press (2000).
14. K. J. Vahala, “Optical Microcavities”, World Scientific, Singapore (2004).
15. A.V. Kavokin, J.J. Baumberg, G. Malpuech and F.P. Laussy, “Microcavities”, Oxford University Press, New York (2007).
16. K. J. Vahala, “Optical Microcavities”, Nature 424, 839-846 (2003).
17. A. Serpengüzel, S. Arnold, G. Griffel and J.A. Lock, “Enhanced coupling to microsphere resonances with optical fibers”, J. Opt. Soc. Am. B 14, 790-795 (1997).
18. Y. Panitchob, G. Senthil Murugan, M. N. Zervas and J. S. Wilkinson, “Q-factor and waveguide-sphere separation effects in waveguide-coupled microsphere resonators”, Proc. SPIE 6793, 67930E (2008).
19. Y. Panitchob, G. Senthil Murugan, M. N. Zervas, P. Horak, S. Berneschi, S. Pelli, G. Nunzi Conti, and J. S. Wilkinson, “Whispering gallery mode spectra of channel waveguide coupled Microspheres”, Opt. Express 16, 11066-11076 (2008).
20. A. Chiasera, Y. Dumeige, P. Féron, M. Ferrari, Y. Jestin, G. Nunzi Conti, S. Pelli, S. Soria and G.C. Righini, “Spherical whispering-gallery-mode microresonators”, Laser & Photonics Reviews, 4: 457–482 (2010).
21. M. Kuwata Gonokami, K. Takeda, H. Yasuda and K. Ema, “Laser-emission from dye-doped polystyrene microsphere”, Japanese J. Appl. Phys., 2, 31, L99–L101 (1992).
22. V.S. Ilchenko, X.S. Yao and L. Maleki, “A fiber-coupled erbium-doped microsphere laser”, Lasers and Electro-Optics, CLEO 2000, 600 (2000)
23. M. Cai, O. Painter, K. J. Vahala and P. C. Sercel, “Fiber-coupled microsphere laser”, Opt. Lett. 25, 1430–1432 (2000)
24. O. Boyraz and B. Jalali, “Demonstration of a silicon Raman laser”, Opt. Express 12, 5269-5273 (2004).

25. O. Boyraz, D. Dimitropoulos and B. Jalali, “Observation of simultaneous Stokes and anti-Stokes emission in a silicon Raman laser”, IEICE Electronic Express 1, 435-441 (2004).
26. O. Boyraz and B. Jalali, “Demonstration of directly modulated silicon Raman laser”, Opt. Express13, 796-800 (2005).
27. H. Rong, R. Jones, A. Liu, O. Cohen, D. Hak, A. Fang and M. Paniccia, “A continuous-wave Raman silicon laser”, Nature 433, 725-728 (2005).
28. H. Rong, S. Xu, O. Cohen, O. Raday, M. Lee, V. Sih and M. Paniccia, “A cascaded silicon Raman laser”, Nature Photon. 2, 170 - 174 (2008).
29. S.F. Preble, Q. Xu and M. Lipson, “Changing the colour of light in a silicon resonator”, Nature Photonics 1, 293-296 (2007).
30. S. Suzuki, Y. Hatakeyama, Y. Kokubun and S. T. Chu, “Precise control of wavelength channel spacing of microring resonator add-drop filter array”, IEEE J. Lightwave Technol., 20, 745–750 (2002).
31. P. Rabiei, W. H. Steier, C. Zhang and L. R. Dalton, “Polymer micro-ring filters and modulators”, IEEE J. Lightwave Technol., 20, 1968–1975 (2002).
32. K. Djordjev, S. J. Choi and P. D. Dapkus, “Microdisk tunable resonant filters and switches”, IEEE Photon. Technol. Lett., 14, 828–830 (2002).
33. A. Serpengüzel, A. Kurt, T. Bilici, Ş. İşçi and Y. O. Yılmaz, “Resonant Channel dropping filter with integrated detector system based on optical fiber coupler and microsphere”, Jpn. J. Appl. Phys., 43, 5878-5881 (2004).
34. T. Bilici, S. Isçi, A. Kurt and A. Serpengüzel, “Microsphere Based Channel Dropping Filter with Integrated Photodetector”, IEEE Photon. Technol. Lett., 16, 476-478 (2004).
35. Y.O. Yilmaz, A. Demir, A. Kurt, and A. Serpengüzel, “Optical Channel Dropping with a Silicon Microsphere”, IEEE Photon. Technol. Lett., 17, 1662-1664 (2005).
36. A. Morand, Y. Zhang, B. Martin, K.P. Huy, D. Amans, P. Benech, J. Verbert, E. Hadji and Jean-Marc Fédéli, “Ultra-compact microdisk resonator filters on SOI substrate”, Opt. Express 14, 12814-12821 (2006).

37. G. Gilardi, A. Serpengüzel, D. Donisi and R. Beccherelli, “Liquid crystal tunable filter based on sapphire microspheres”, Opt. Lett. 34, 3253-3255 (2009).
38. E. Hüseyinoglu, M.S. Murib, A. Serpengüzel and R. Beccherelli, “Ruby microsphere and liquid crystal based tunable optical filter”, LEOS Annual Meeting Conference Proceedings, 2009. LEOS '09. IEEE, 191-192 (2009).
39. G. Ctistis, E. Yüce, A. Hartsuiker, J. Claudon, M. Bazin, J. M. Gérard and W. L. Vos, “Ultimate fast optical switching of a planar microcavity in the telecom wavelength range”, Appl. Phys. Lett. 98, 161114 1-3 (2011).
40. Q. Xu, S. Manipatruni, B. Schmidt, J. Shakya and M. Lipson, “12.5 Gbit/s carrier-injection-based silicon micro-ring silicon modulators”, Opt. Express 15, 430-436 (2007).
41. L. Liu, J. Van Campenhout, G. Roelkens, R.A. Soref, D. Van Thourhout, P. Rojo-Romeo, P. Regreny, C. Seassal, Jean-Marc Fédéli and R. Baets, “Carrier-injection-based electro-optic modulator on silicon-on-insulator with a heterogeneously integrated III-V microdisk cavity”, Opt. Lett. 33, 2518-2520 (2008).
42. E. Yüce, O. Gürlü and A. Serpengüzel, “Optical modulation with silicon microspheres”, IEEE Photon. Technol. Lett., 21, 1481-1483 (2009).
43. S. Arnold and F. Vollmer, “Shift of whispering gallery modes in microspheres by protein absorption”, Optics Letters, 28, 272-274 (2003).
44. F. Vollmer, S. Arnold, D. Braun, I. Teraoka and A. Libchaber, “Multiplexed DNA Quantification by Spectroscopic Shift of Two Microsphere Cavities”, Biophysical J. 85, 1974-1979 (2003).
45. A. Demir and A. Serpengüzel, “Silica Microspheres for Biomolecular Detection Applications”, IEEE Proc. on Nanobiotechnol., 152, 105-107 (2005).
46. I. M. White, “Tuning whispering gallery modes in optical microspheres with chemical etching”, Opt. Express, 13, 10754-10759 (2005).

47. A.M. Armani, D.K. Armani, B. Min, K.J. Vahala and S.M. Spillane, “Ultra-high-Q microcavity operation in H_2O and D_2O”, Appl. Phys. Lett. 87, 151118 1-3 (2005).
48. Andrea M. Armani and Kerry J. Vahala, “Heavy water detection using ultra-high-Q microcavities”, Opt. Lett.31, 1896-1898 (2006).
49. D. Keng, S.R. McAnanama, I. Teraoka and S. Arnold, “Resonance fluctuations of a whispering gallery mode biosensor by particles undergoing Brownian motion”, Appl. Phys. Lett. 91 (2007).
50. T. Ioppolo, M. Kozhevnikov, V. Stepaniuk, M. V. Ötügen and V. Sheverev, “Micro-optical force sensor concept based on whispering gallery mode resonators”, Appl. Opt. 47, 3009-3014 (2008).
51. F. Vollmer and S. Arnold, “Whispering-gallery-mode biosensing: label-free detection down to single molecules”, Nature Methods - 5, 591 - 596 (2008).
52. P. Del Haye, A. Schliesser, O. Arcizet, T. Wilkins, R. Holzwarth and T.J. Kippenberg, “Optical frequency comb generation from a monolithic microresonator”, Nature 450, 1214-1217 (2007).
53. O.D. Lavrentovich, I. Lazo and O.P. Pishnyak, “Nonlinear electrophoresis of dielectric and metal spheres in a nematic liquid crystal”, Nature 467, 947-950 (2010).
54. S.E. Miller, “Integrated Optics: An Introduction”, The Bell System Technical J., 48, 2059–2068 (1969).
55. L. A. Coldren and S. W. Corzine, “Diode Lasers and Photonic Integrated Circuits”, Wiley-Interscience, New Jersey (1995).
56. Q. Xu and M. Lipson, “All-optical logic based on silicon micro-ring resonators”, Opt. Express 15, 924-929 (2007).
57. A. Serpengüzel, A. Kurt and U.K. Ayaz, “Silicon microspheres for electronic and photonic integration”, Photon. Nanostructur. Fundam. Appl. 6, 179–182 (2008).
58. A. Serpengüzel and A. Demir, “Silicon Microspheres for near-IR communication applications”, Semicond. Sci. Technol. 23, 064009 (2008).

59. L. Pavesi, “Will silicon be the photonic material of the third millennium?”, J. Phys. Condens. Matter, 15, (2003).
60. B. Jalali and S. Fathpour, “Silicon Photonics”, J. Lightwave Technol., 24, 4600-4615 (2006).
61. L.V. Lorenz, “Lysbevaege i og uder en plane lysbolger belyst kluge”, Vidensk. Selk. Skr. 6, 1–62 (1890).
62. G. Mie, “Beiträge zur Optik trüber Medien, speziell kolloidaler Metallösungen”, Annalen der Physik, 330, 377–445 (1908).
63. J.A. Lock and G. Gouesbet, “Generalized Lorenz-Mie theory and applications”, J. Quant Spectrosc Radiat Transfer 110, 800-807 (2009).
64. E. Hecht, “Optics”, Addison Wesley Longman Inc., London (2002).
65. P. Chýlek, “Resonance structure of Mie scattering: distance between resonances”, J. Opt. Soc. Am. A 7, 1609-1613 (1990).
66. G.T. Reed and A.P. Knights, “Silicon Photonics”, John Wiley & Sons, Ltd., West Sussex (2004).
67. A. Serpengüzel and O. Akatlar, “Silicon microspheres for wavelength division multiplexing in the THz band”, Proc. SPIE 6125, 61250T 1-4 (2006).
68. A. Serpengüzel and A.W. Poon, “Optical Processes in Microparticles and Nanostructures”, World Scientific, Singapore (2011).
69. S.C. Hill, A.C. Hill and P.W. Barber, “Light scattering by size/shape distributions of soil particles and spheroids”, Appl. Opt. 23,1025-1031 (1984).
70. H.-M. Tzeng, M.B. Long, R.K. Chang and P.W. Barber, “Laser-induced shape distortions of flowing droplets deduced from morphology-dependent resonances in fluorescence spectra”. Opt. Lett. 10, 209-211 (1985).
71. G. Chen, R.K. Chang, S.C. Hill and P.W. Barber, “Frequency splitting of degenerate spherical cavity modes: stimulated Raman scattering spectrum of deformed droplets”, Opt. Lett. 16, 1269-1271 (1991).
72. G. Chen, M. Mazumder, Y.R. Chemla, A. Serpengüzel and R.K. Chang, “Wavelength variation of laser emission along the entire rim of slightly deformed microdroplets”, Opt. Lett. 19, 1993-1995 (1993).